Soluble Amyloid β-Oligomers Affect Dielectric Membrane Properties by Bilayer Insertion and Domain Formation: Implications for Cell Toxicity

Gintaras Valincius,* Frank Heinrich,†‡ Rima Budvytyte,* David J. Vanderah,§ Duncan J. McGillivray,¶ Yuri Sokolov,|| James E. Hall,|| and Mathias Lösche†‡
*Department of Bioelectrochemistry and Biospectroscopy, Institute of Biochemistry, Vilnius, Lithuania; †Physics Department, Carnegie Mellon University, Pittsburgh, Pennsylvania; ‡Center for Neutron Research, National Institute of Standards and Technology (NIST), Gaithersburg, Maryland; §Chemical Sciences and Technology Laboratory, NIST, Gaithersburg, Maryland; ¶Department of Chemistry, The University of Auckland, Auckland, New Zealand; and ||Department of Physiology and Biophysics, School of Medicine, University of California at Irvine, Irvine, California

ABSTRACT It is well established that Alzheimer's amyloid β-peptides reduce the membrane barrier to ion transport. The prevailing model ascribes the resulting interference with ion homeostasis to the formation of peptide pores across the bilayer. In this work, we examine the interaction of soluble prefibrillar amyloid β (Aβ_{1-42})-oligomers with bilayer models, observing also dramatic increases in ion current at micromolar peptide concentrations. We demonstrate that the Aβ-induced ion conductances across free-standing membranes and across substrate-supported "tethered" bilayers are quantitatively similar and depend on membrane composition. However, characteristic signatures of the molecular transport mechanism were distinctly different from ion transfer through water-filled pores, as shown by a quantitative comparison of the membrane response to Aβ-oligomers and to the bacterial toxin α-hemolysin. Neutron reflection from tethered membranes showed that Aβ-oligomers insert into the bilayer, affecting both membrane leaflets. By measuring the capacitance of peptide-free membranes, as well as their geometrical thicknesses, the dielectric constants in the aliphatic cores of 1,2-dioleoyl-*sn*-glycero-3-phosphocholine and 1,2-diphytanoyl-*sn*-glycero-3-phosphocholine bilayers were determined to be $\varepsilon = 2.8$ and 2.2, respectively. The magnitude of the Aβ-induced increase in ε indicates that Aβ-oligomers affect membranes by inducing lateral heterogeneity in the bilayers, but an increase in the water content of the bilayers was not observed. The activation energy for Aβ-induced ion transport across the membrane is at least three times higher than that measured for membranes reconstituted with α-hemolysin pores, $E_a = 36.8$ vs. 9.9 kJ/mol, indicating that the molecular mechanisms underlying both transport processes are fundamentally different. The Aβ-induced membrane conductance shows a nonlinear dependence on the peptide concentration in the membrane. Moreover, E_a depends on peptide concentration. These observations suggest that cooperativity and/or conformational changes of the Aβ-oligomer particles upon transfer from the aqueous to the hydrocarbon environment play a prominent role in the interaction of the peptide with the membrane. A model in which Aβ-oligomers insert into the hydrophobic core of the membrane—where they lead to a local increase in ε and a concomitant reduction of the membrane barrier—describes the experimental data quantitatively.

INTRODUCTION

The correlation between neurodegenerative disease and amyloid aggregation in brain tissue has long been established (1): fibrillar plaques associated with dead or damaged neurons are a characteristic observation in postmortem brains of patients suffering from Alzheimer's disease (AD) and Parkinson's disease. Consequently, the amyloid hypothesis links protein aggregation into fibrillar structures with a cascade of events that leads ultimately to neurodegeneration (2). However, the question of whether the deposits are caused by, or, rather, lead to, neurodegeneration has been vigorously debated for a century and remains unanswered (3), at least partially due to the lack of a viable molecular-scale approach to its investigation.

One reason for the persistence of this debate lies in the variety of guises in which amyloid peptides and their aggregation products occur in vivo. First, there is a variability in the cleavage sites in the proteolytic processing of the amyloid precursor protein (APP) by various secretases (4), yielding product peptides of different lengths, i.e., Aβ_{1-40} and Aβ_{1-42}. Second, their sequential oligomerization into larger aggregates leads to different physical forms—monomers, oligomers, protofibrils, fibrils, and fibrillar tangles—that may be in dynamic equilibrium and may each contribute differently to pathogenicity. Much recent work has been dedicated to structural characterization of amyloid aggregation products and attempts to unravel their reactive pathways (5–9). Indeed, evidence has recently accrued that Aβ toxicity resides primarily with a soluble oligomeric form of the peptide rather than Aβ-monomers or mature fibrils (10–17). In view of the lack of understanding of the molecular origin of Aβ toxicity, it is therefore timely to concentrate on molecular biophysical studies of the properties of Aβ-oligomer particles (18).

Because Aβ peptides implicated in AD and the aggregation products of other misfolded peptides implicated in related peptide misfolding pathologies (19)—such as α-synuclein (Parkinson's disease), polyglutamine (Huntington's disease), islet amyloid polypeptide (type 2 diabetes

---

Submitted April 1, 2008, and accepted for publication May 9, 2008.

Address reprint requests to Mathias Lösche, Physics Department, Carnegie Mellon University, 5000 Forbes Ave., Pittsburgh, PA 15213-3890. Tel.: 412-268-2735; Fax: 412-268-8252; E-mail: quench@cmu.edu.

Editor: Thomas J. McIntosh.

0006-3495/08/11/4845/17 $2.00

doi: 10.1529/biophysj.108.130997

mellitus)—affect very different tissues in patients and because misfolded peptide oligomers appear to translocate membranes easily, it is intriguing to speculate that oligomer interaction with bilayer membranes plays a major part in determining the physiological roles of these peptide oligomers on the molecular scale (4). In fact, soluble Aβ_{1-42}-oligomers destabilize the membrane of giant unilamellar vesicles (20). It is not surprising that the poration of membranes by amyloid aggregates has been a major recurring theme in explaining amyloid toxicity ever since a first report of membrane channels induced by amyloid peptide was published (21). After all, membrane pores formed by amyloid oligomers or even specific channel structures similar to those formed by bacterial exotoxins, would greatly disturb Ca^{2+} homeostasis, thereby providing a plausible mechanism for oligomer toxicity (22). The amyloid channel hypothesis has also been fueled by the observation of annular peptide aggregates, for example, in atomic force microscopy (AFM) studies of substrate-supported membranes (23,24), which suggest the formation of pores. However, the preparation protocol invokes self-assembly from premixed lipid/peptide dispersions, possibly limiting their physiological significance, particularly because the incubation of preformed bilayers with amyloid solution yields peptide structures that are morphologically distinct (25).

Evidence for ion channels from membrane conductivity measurements is also not yet conclusive. On the one hand, there are reports of conductance patters in bilayers (23,26) and clamped cell membranes (27) that resemble the single-channel behavior observed in exotoxin studies (28) in free-standing bilayers (black lipid membranes (BLMs); Fig. 1 *A*). On the other hand, it has been demonstrated in both BLMs and cultured rat basophilic leukemia cells that soluble Aβ_{1-42}-oligomers increase the conductance of membranes in a way inconsistent with the formation of ion channels (15,17). These studies show that the oligomers affect the lipid membranes by lowering the dielectric barrier of the bilayer. Most intriguing, in the BLM studies that investigated compositionally well-defined lipid bilayers, it was found that membranes composed of lipids with high compressibility, such as phospholipids with unsaturated chains, are more amenable to peptide oligomer effects than those composed of low-compressible lipids, such as phospholipids with phytanoyl chains or sphingomyelins (17).

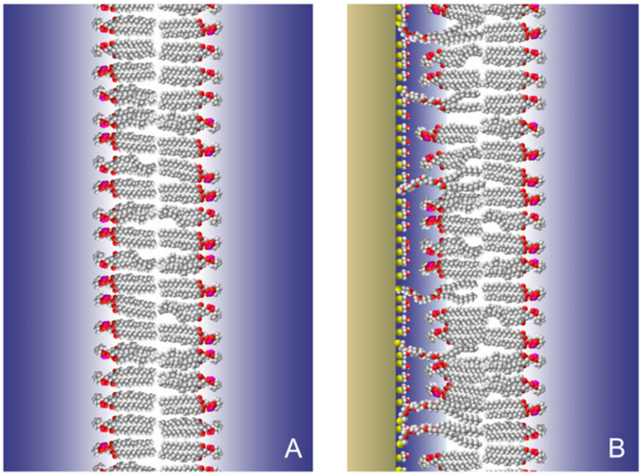

FIGURE 1 Schematic representation of the synthetic lipid bilayer systems used in this study. (*A*) Free-standing BLM. (*B*) Solid-supported stBLM. Molecular details of stBLMs, specifically the geometry and hydration of the submembrane space between the bilayer and the inorganic substrate, have been established with NR in earlier work (40,41) and are drawn to scale.

Beyond interference with ion homeostasis by conductance increases, subtle alterations of membrane properties may play more complex roles in AD etiology. Seelig and co-workers recognized early on the interdependence of membrane exposure of Aβ and peptide conformation (see Terzi et al. (29) and work cited therein). McLaurin and co-workers continue to investigate the role of membranes in peptide fibrillogenesis (30), and others are pursuing this line of research as well, with progressively deeper insight into molecular details (31,32). Even more intriguing are aspects of membrane microstructure and their implications for disease. The role of lipid material properties in the formation of microheterogeneity (the ''raft hypothesis'') was recently reviewed, with a discussion of their role in the recruitment of peptides (33). In the context of AD, the role of ''lipid rafts'' in cell signaling may be of secondary relevance, but there have been reports implicating rafts in the amyloidogenic processing of amyloid precursor protein by both β-secretase and γ-secretase (34–36). In the light of those findings, the interaction of Aβ with rafts becomes very relevant. Indeed, if Aβ-peptide affects the formation or balance of microheterogeneities in membranes, this might provide a fatal amplification mechanism for pathogenesis.

Here, we investigate supported membranes (37–39) for their structural and electrochemical response to soluble Aβ-oligomers to study the molecular-scale events that govern Aβ-oligomer interaction with bilayers. We have optimized a supported bilayer system, the sparsely tethered bilayer lipid membrane (stBLM, see schematic representation in Fig. 1 *B*), in which a lipopolymer tether anchors a bilayer structure to the gold-coated surface of a Si wafer (40). Neutron reflectometry (NR) has been used to determine the molecular-scale structure of these systems. In the preparation of stBLMs, the tether molecules are laterally diluted by a hydrophilically terminated thiol, β-mercaptoethanol (βME), resulting in a molecularly thin ($d \approx 15$ Å), stable hydration layer between the membrane and the gold layer (40,41). For biophysical work, stBLMs offer the advantage of a well defined model system that is amenable to a multitude of well established, molecular-scale characterization techniques. For example, stBLMs were structurally characterized in detail using NR (40). Of equal importance, the synergy between NR and electrochemical impedance spectroscopy (EIS) has been demonstrated (41). The combined metrologies couple structural characterization (NR) with the assessment of protein function in the membrane (EIS). For example, a recent investigation of the formation of nanoscale pores in stBLMs by the exotoxin α-hemolysin (αHL) from *Staphylococcus aureus* (42) using these techniques (43) enables us to make a quantitative comparison of the impact of Aβ-oligomers with that of αHL in this study. Taken together, these results on stBLMs also afford a comparison with the effects of Aβ-oligomers on free-standing BLMs and cell membranes. In the context of Alzheimer's etiology, this is important, because monitoring membrane conductivity provides access to molecular details of the interaction between Aβ_{1-42}-oligomers and the bilayer, whose dielectric properties are essential for the homeostasis of ions, as well as the passive and active ion transport that governs signal conduction along the axon. It is conceivable that an increase of membrane permeability by Aβ-oligomers triggers a complex network of biochemical cascades, thus leading to a spectrum of pathological symptoms. A better understanding of molecular-level effects of Aβ-oligomers on membranes is therefore critically needed for the development of early-detection mechanisms for AD, as well as for therapeutic approaches.

MATERIALS AND METHODS

Materials and sample preparation

20-tetradecyloxy-3,6,9,12,15,18,22-heptaoxahexatricontane-1-thiol (WC14) was synthesized and characterized as described (supporting information for McGillivray et al. (40)). βME, from Sigma-Aldrich (St. Louis, MO), was distilled before use. 1,2-diphytanoyl-*sn*-gly-cero-3-phosphatidylcholine, 1,2-dioleoyl-*sn*-glycero-3-phosphatidylcholine, 1,2-dimyristoyl-*sn*-glycero-3-phosphatidylcholine, and 1,2-perdeuterodimyristoyl-*sn*-glycero-3-phosphatidylcholine (DPhyPC, DOPC, DMPC, and DMPC-d_{54}, respectively) were from Avanti Polar Lipids (Alabaster, AL). H_2O was purified in a Millipore (Billerica, MA) UHQ reagent-grade water purification system. D_2O (99.9% isotope purity) was from Cambridge Isotopes Laboratory (Andover, MA). Salts, buffers, organic solvents, and squalene from Sigma-Aldrich, J. T. Baker, or Mallinkrodt-Baker were of at least ACS reagent or analytical reagent grade.

Planar lipid bilayers

Free-standing BLMs were formed at room temperature by the union of two monolayers, as previously described (15,17). Briefly, lipid monolayers were formed on aqueous solutions that contained various concentrations of KCl or NaCl buffered with 10 mM HEPES-Tris to pH 7.4. They were apposed over a hole (diameter ~150 μm) in a 15-μm-thick Teflon partition that separated the two aqueous phases. The hole, punched by an electric spark, was precoated with a 2.5% solution of squalene in *n*-pentane. Bilayer formation was monitored by measuring capacitance. Silver/silver chloride electrodes were used to apply voltages and record currents across the bilayer. One chamber potential was taken as ground and additions were made to the other chamber. Solutions were stirred with magnetic stirring bars for ~30 s after additions. Voltages were generated and currents digitized at a resolution of 12 bits by an AD Lab ADC/DAC board controlled by JCLAMP (SciSoft, New Haven, CT) driving a PCI-6024E board (National Instruments, Austin, TX). Currents were transduced by an Axopatch 200A amplifier (Axon Instruments, Foster City, CA) connected to the board. For measurements of the membrane conductance, a voltage ramp protocol ($U = -150$ to $+150$ mV at 60 mV/s) was applied.

Tethered lipid bilayers

stBLMs were formed on thin gold films (thickness ~10 nm for NR and ~200 nm for EIS), deposited by magnetron sputtering (Auto A306, BOC Edwards, Crawley, United Kingdom) on *n*-doped, [100]-cut Si wafers (El-Cat, Waldwick, NJ, or Silicon, Boise, ID) precoated with an ~2-nm-thick Cr adhesion layer, as described (44). Typically, the gold films had an RMS surface roughness of 0.5 nm, as measured by x-ray reflectometry (Bruker AXS, Madison, WI). Similar values were determined by AFM: ~0.5 nm for thin gold films and ~0.8 nm for the 200-nm gold films. The thickness uniformity across the surface was ±3% or better, as determined by ellipsometry.

The formation of stBLMs is a two-step process that involves the coadsorption of WC14 with βME, followed by incubation with an ethanolic phospholipid solution and rapid solvent exchange (38). 1), Mixed self-assembled monolayers were prepared by exposing magnetron-sputtered Au films to solutions of WC14:βME (3:7 mol/mol, 0.2 mM total concentration) in 99.5% ethanol for >12 h. 2), stBLMs were completed by incubation of the moderately hydrophobic surface with a concentrated (~10 mM) ethanolic solution of a phospholipid that was rapidly, within ~5 s, replaced by vigorous injection of aqueous buffer (0.1 M NaCl, 0.01 M phosphate, pH 7.0–7.5) into the sample cell. This rapid solvent-exchange procedure leads to the formation of a complete and electrically insulating bilayer with a residual conductance of 1–2 $\mu S/cm^2$ (40).

Amyloid oligomer particles

Aβ_{1-42}-oligomers were prepared at the University of California, Irvine, as described (15,17). Lyophilized peptides were resuspended in 50% acetonitrile in water and relyophilized. Soluble oligomers were prepared by dissolving 1.0 mg of peptide in 400 μL hexafluoroisopropanol at room temperature. Of the resulting seedless solution, 100 μL was added to 700 μL H_2O in a siliconized Eppendorf tube. After 10–20 min incubation, samples were centrifuged for 15 min at 14,000 × *g*. The supernatant (pH 2.8–3.5) was transferred into a new siliconized tube and the hexafluoroisopropanol was evaporated in a gentle N_2 stream. Samples were then stirred at 500 rpm using a Teflon-coated micro stir bar for 24–48 h at room temperature. Aliquots were taken at 6- to 12-h intervals for testing in dot blots with the antioligomer antibody A11 (14). Samples were also characterized using electron microscopy and size exclusion chromatography (45). Freshly prepared peptide oligomers were shipped overnight to the NIST Center for Neutron Research for characterization in EIS and NR experiments. As described in detail below, the concentration dependence of Aβ_{1-42}-oligomers on EI spectra can be used to monitor oligomer activity. In split batches, the activity of oligomer preparations determined with EIS on stBLMs correlated well with the oligomer activity measured on free-standing BLMs at the University of California.

Electrochemical impedance spectroscopy

EIS measurements were performed using a Solartron (Farnborough, United Kingdom) system (1287A potentiostat and 1260 frequency response analyzer) between 1.0 and 65,000 Hz, with 10 logarithmically distributed measurements per decade. Data were fitted using ZView (Scribner Associates, Southern Pines, NC). Gold-coated silicon wafers (20 × 40 mm) served as the working electrodes in a setup that allowed simultaneous EIS measurements in six distinct electrochemical cells (V (volume) $\approx$ 250–300 μL) on each wafer, with their surface areas ($A_{el} \approx 0.33$ cm^2) on the gold film confined by Viton O-rings. Copper contrast was used to measure the geometric electrode surface area (46). EIS data were normalized to A_{el} and the roughness factor β was estimated from the gold surface oxidation/oxide stripping charge (47). A saturated silver-silver chloride (Ag/AgCl/NaCl (aq,sat)) microelectrode (M-401F, Microelectrodes, Bedford, NH) was used as reference. The auxiliary electrode was a 0.25-mm-diameter platinum wire (99.99% purity, Aldrich) coiled around the barrel of the reference electrode.

The distance between the tip of the reference and the working gold electrode surface was set to 2–3 mm. All measurements were carried out at 0 V bias versus the reference electrode at 21 ± 1°C in aerated solutions.

Neutron reflection and data analysis

NR measurements were performed at the AND/R (48) at the NIST Center for Neutron Research. The resilience of the stBLMs permitted the NR characterization of the as-prepared membrane at various solvent contrasts, followed by measurement of the stBLM incubated with Aβ-oligomers, all with the same physical sample. Also, since the incubation with the peptide was performed in situ on the neutron spectrometer, all reflectivity curves were measured on exactly the same sample footprint. With the substrate and membrane structures thus established in a first step, structural changes due to amyloid incubation were studied in detail.

All stBLMs were prepared with a single phosphatidylcholine species: DOPC, DPhyPC, DMPC, or DMPC-d$_{54}$. With hydrogenated phospholipid, the inner and outer bilayer leaflets are identical in neutron scattering length density (nSLD), and cannot be discriminated. On the other hand, using DMPC-d$_{54}$ enabled a discrimination of the stBLM leaflets because the outer leaflet is composed of 100% deuterated polymethylene, whereas the inner leaflet is composed of a mixture of hydrogenated polymethylene (of the WC14) and deuterated polymethylene (of DMPC-d$_{54}$ intercalating the tethered WC14 self-assembled monolayer). Further neutron contrast is most easily achieved by using buffers of various isotopic compositions for the solution bathing the stBLM. We showed in earlier work that stBLMs are stable over days (at least) and are also stable against buffer exchange. Exploiting this stability, each of the as-prepared stBLMs was sequentially characterized in three different solvent contrasts using buffer based upon D_2O, H_2O, or a mixture of both with, e.g., an nSLD, $\rho_n \approx 4 \times 10^{-6}$ Å^{-2} (''CM4''). This basic characterization of the neat stBLM was followed by continuous incubation with Aβ_{1-42}-oligomers at the desired peptide concentration and further NR measurements with peptide solutions in buffers of different isotopic constitution. Reversibility of the peptide interaction with the lipid bilayer was routinely probed in a final NR measurement after extensive rinsing.

Data analysis was performed in terms of slab models, or ''box'' models (49), using *ga_refl* (50), in which the reflectivity from a model nSLD profile is computed using an optical matrix formalism based on Parratt's recursion algorithm (51). Isostructural samples with distinct isotopic contrast were simultaneously fitted by consistently refining the corresponding nSLD profiles, which were parameterized in terms of the underlying molecular structures (52), an approach termed ''composition-space refinement'' (53). In the implementation used in this work, the model contains the following sequence of layers to represent the sample system: (semi-infinite) Si wafer, silicon oxide, chromium, gold, the hydrated hexa(ethylene oxide) (HEO) spacer, the inner leaflet of the bilayer, the outer leaflet of the bilayer, the outer headgroup layer, and the bulk solvent. The model allows all organic layers to comprise solvent (thought to either hydrate organic moieties such as a phospholipid headgroups or to form solvent-filled defect pockets, as in the case of the hydrophobic chain layer). Thus, solvent contributes to the average scattering power of each layer according to the nSLD of the bulk solvent multiplied by its volume fraction in the layer (which is zero for a defect-free stBLM). Both lipid leaflets in the stBLM model were constrained to the same hydrophobic thickness, because in high-quality bilayers such as those investigated in this work, the two thicknesses are highly correlated. The inner headgroup layer of the lipid membrane was indistinguishable from the HEO tether at all solvent contrasts, and was therefore not separately modeled.

The stability of the stBLMs was confirmed by the fact that any of the data sets at different solvent contrasts can be well described by the same parameter set in the refined composition-space model (40,41). Moreover, if data sets representing different neutron contrasts were fitted independently of each other, this yielded consistent parameter values, albeit with larger uncertainties. The final analysis of an experiment—reported in the following section in terms of best-fit parameters and associated uncertainties—was therefore always performed in a simultaneous fit to all reflectivity curves taken on a particular bilayer sample. In these results, identical parameter values describe those regions in the sample invariant to solvent exchange or peptide oligomer incubation (i.e., the inorganic multilayer substrate). In contrast, regions that are solvent-accessible and/or affected by the peptide are described by parameter sets that are mutually consistent in that they derive from a unique molecular structure that translates into distinct nSLDs by attaching the appropriate scattering lengths to its atomic composition.

RESULTS

Neutron reflection from tethered bilayer membranes

Only protonated Aβ_{1-42} was available in these experiments. Because the contrast of the peptides against the membrane structure is low, the particles could not be directly located at the membrane in a structural model. On the other hand, the membrane structural properties were critically affected by Aβ_{1-42}-oligomer incubation, which led to significant and reversible changes in the stBLM structural parameters. Here, we use this information for a quantitative assessment of the membrane dielectric responses. Initial NR experiments with fully hydrogenated stBLMs suggested a small, reversible thinning of the hydrophobic core of the bilayers, which depended in its extent on the nature of the lipid, peptide concentration, and the activity of the Aβ_{1-42}-oligomer preparation. Subsequent measurements employing chain-perdeuterated DMPC-d$_{54}$ showed these changes in more detail. We will therefore concentrate here on experiments with the chain-labeled membrane component.

The stBLM prepared from DMPC-d$_{54}$ was characterized with NR in an extended set of measurements. The as-prepared membrane was first characterized at three solvent contrasts, then subjected to soluble Aβ_{1-42}-oligomers at $c_p = 2$ μM in D_2O-based buffer and characterized at two more solvent contrasts; subjected at $c_p = 6$ μM and characterized at three more solvent contrasts; subjected at $c_p = 12$ μM and characterized at two more solvent contrasts; was and, finally, rinsed with peptide-free buffer and characterized again at three solvent contrasts. The entire experiment used around four days of neutron beamtime. In Fig. 2, we present exemplary NR data sets measured in H_2O-based buffer, as well as the respective model fits, for the neat stBLM and the same stBLM incubated with soluble Aβ_{1-42}-oligomers at the final peptide concentration of $c_p = 12$ μM. The normalized residuals (Fig. 2, *lower inset*) emphasize the reflectivity changes induced by the peptide oligomers. They also demonstrate the almost complete reversal of those effects upon rinsing with peptide-free buffer. Because the stBLM was prepared from (fully hydrogenated) WC14/βME (3:7 in the adsorption solution) and completed with DMPC-d$_{54}$, the inner and outer hydrophobic sheaths of the bilayer show different nSLD, which are easily distinguished in nSLD profiles (Fig. 2, *upper inset*). A close inspection of these profiles shows that Aβ-oligomer incubation increases the nSLD of

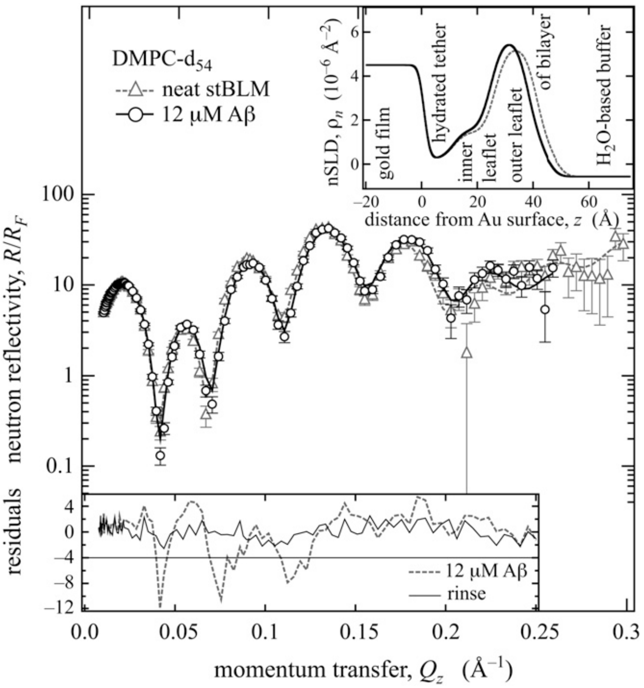

FIGURE 2 Neutron reflection of an stBLM (WC14/βME = 3:7 + DMPC-d$_{54}$) and changes in bilayer structure introduced by Aβ_{1-42}-oligomers. Out of a multitude of NR data sets collected with the same bilayer with various solvent contrasts (see text), two exemplary data sets (as-prepared stBLM and the same stBLM in contact with dissolved Aβ-oligomers, $c_p = 12$ μM of peptide) are shown in the main panel. Both data sets were measured in H_2O-based buffer. The prominently visible interference patterns are primarily due to the gold layer. If visually inspected, any organic interface layer alters this interference pattern only slightly. However, these changes are much larger than the precision of the data (error bars are shown for every data point; at low Q_z, errors are generally much smaller than plot symbols). (*Lower inset*) The significance of the changes in reflectivity due to bilayers with different structure is emphasized in a residuals plot in which deviations of the data set shown as black circles (12 μM Aβ) from the data shown as gray triangles (neat stBLM) are plotted. The residuals of an NR spectrum for the amyloid-incubated stBLM after a buffer rinse are also shown (*thin black line*), indicating the reversibility of structural changes. The upper inset shows the modeled nSLD profiles of the organic interface layers (Si substrate, SiO$_x$ layer, Cr bonding layer, and Au layer are partially omitted). These models were derived from multiple solvent contrasts for which the data are not shown. The reflectivities computed for the nSLD profiles shown overlay the data points in the main panel as solid (*black*) or broken (*gray*) lines. A color version of this figure is available in Data S1.

the hydrophobic slabs, and shifts the peak nSLD closer to the substrate surface. Table 1 lists the model parameters obtained from a simultaneous fit to all NR data. A more complete account that includes the inorganic substrate and confidence-limit estimates based on a Monte Carlo resampling technique is provided in Supplementary Material, Data S1.

The bilayer shows no increase of solvent content in the hydrophobic slabs that would indicate the formation of solvent-filled defects in the bilayer by the peptide. The initial nSLDs of the inner and outer leaflets were $\rho_n = 1.60 \pm 0.13 \times 10^{-6}$ Å^{-2} and $\rho_n = 5.55 \pm 0.34 \times 10^{-6}$ Å^{-2}, respectively. The difference derives from the fact that the inner leaflet incorporates the (hydrogenated) lipid anchor, WC14. Assuming an alkyl nSLD of $\rho_n = -0.4 \times 10^{-6}$ Å^{-2}, typical for chains in a fluid bilayer, and equal mass densities in the inner and outer leaflets, we estimate the volume fraction of DMPC-d$_{54}$ in the inner lipid leaflet to be 34 ± 4% in the as-prepared stBLM. Incubation with soluble Aβ_{1-42}-oligomers led to significant changes of the nSLD in both lipid leaflets for all peptide concentrations applied in the experiment. As for fully hydrogenated DOPC-based stBLMs (see below), we observe a thinning of the membrane. For the deuterated bilayer, this thinning amounts to $\Delta d = -1.4 \pm 0.4$ Å and -3.0 ± 0.4 Å at $c_p = 6$ μM and $c_p = 12$ μM, respectively. The material density of the headgroup (i.e., its volume fraction within the layer next to the bulk solvent) increased by 8 ± 4%, independent of the peptide concentration. Upon rinsing with buffer, all structural effects induced by Aβ_{1-42}-oligomers on the stBLM were reversible within the confidence limits of the experiment. Trial models that included an adsorbed peptide layer at the interface between the bilayer headgroups and the bulk solvent did not indicate any significant volume fraction of adsorbed material for any of the peptide concentrations. The detection limits are estimated to be <10% for the volume fraction and ~10 Å for the thickness of such a hypothetical peptide layer. This indicates that the peptide is not peripherally adsorbed on the membrane surface or inserted into the membrane and extending into the adjacent buffer. Rather, the model suggests that peptide oligomers insert fully into the hydrophobic membrane core.

In terms of nSLD changes, fully hydrogenated stBLMs based upon DOPC and DPhyPC showed smaller responses than deuterated stBLMs to the incubation with Aβ_{1-42}-oligomers. Complex data sets that were collected in procedures similar to that described above for DMPC-d$_{54}$-based stBLMs are partially presented in Figs. 3 and 4. The corresponding model fits are given in Tables 2 and 3. These models show that nSLD shows little response to peptide incubation. The one notable exception is the nSLDs of the hydrophobic bilayer interior, which increased slightly due to peptide insertion. On the other hand, comparison of the nSLD profiles in different solvent contrasts shows unmistakably that peptide incubation didn't affect the water content of the bilayers: consistent with the DMPC-d$_{54}$ results, both leaflets in both the DOPC and DPhyPC bilayers remained solvent-free within an uncertainty of 3%.

A significant difference in structural response of DPhyPC and DOPC to peptide incubation was observed in terms of the membrane thickness, which remained constant for DPhyPC but decreased substantially for DOPC. Peptide concentrations of $c_p = 6$ μM and 12 μM reduced the DOPC membrane thickness by $\Delta d = -2.4$ Å and -3.8 Å, respectively. This is substantially more than the thickness reduction observed for the saturated phospholipid, DMPC. As with DMPC stBLMs, the thinning relaxed completely after the bilayer was rinsed with aqueous buffer.

TABLE 1 Model parameters describing changes of an stBLM structure (WC14/βME = 3:7 + DMPC-d_{54}) upon incubation with soluble prefibrillar Aβ_{1-42}-oligomers

	Neat bilayer	Change from neat bilayer	2 μM Aβ_{1-42}	6 μM Aβ_{1-42}	12 μM Aβ_{1-42}	Rinse
Thickness of tether layer (Å)	10.5 ± 1.7					
Thickness of each bilayer leaflet (Å)	14.9 ± 1.2	Change:	0.0 ± 0.2	–0.7 ± 0.2	–1.5 ± 0.2	–0.3 ± 0.2
Thickness of headgroup layer (Å)	7.0 (fixed)					
Volume fraction of tether in layer	0.69 ± 0.02					
Volume fraction of inner lipid leaflet	0.93 ± 0.04	Change:	–0.01 ± 0.02	0.0 ± 0.03	+0.02 ± 0.03	+0.01 ± 0.03
Volume fraction of outer lipid leaflet	0.95 ± 0.02	Change:	+0.01 ± 0.02	–0.01 ± 0.03	–0.01 ± 0.03	0.0 ± 0.03
Volume fraction of outer headgroup	0.59 ± 0.09	Change:	+0.08 ± 0.04	+0.06 ± 0.04	+0.08 ± 0.05	0.0 ± 0.05
nSLD of inner lipid leaflet (10^{-6} Å^{-2})	1.60 ± 0.13	Change:	+0.29 ± 0.09	+0.24 ± 0.09	+0.08 ± 0.09	+0.03 ± 0.10
nSLD of outer lipid leaflet (10^{-6} Å^{-2})	5.55 ± 0.34	Change:	+0.29 ± 0.08	+0.49 ± 0.11	+0.48 ± 0.18	+0.09 ± 0.11
Substrate roughness (Å)	3.96 ± 1.29					
Bilayer roughness (Å)	7.89 ± 1.99					
χ^2	5.4, 2.5, 1.6		3.7, 2.4	2.6, 2.0, 1.8	2.4, 2.0	3.0, 1.8

Electrochemical impedance spectroscopy of tethered bilayer lipid membranes

Incubation of stBLMs with soluble Aβ_{1-42}-oligomers results in spectral changes exemplified in Bode diagrams, as seen for DOPC in Fig. 5. Aβ leads to a characteristic reduction of the membrane impedance, Z, at low frequency, f (Fig. 5 *A*). The onset of the associated plateau in $|Z(f)|$ coincides with a maximum of the phase angle, φ (Fig. 5 *B*) and occurs at progressively higher f as c_p increases. Similar spectral signatures have been reported after membrane incubation with ionophores (38,54), pore-forming toxins (55), and phospholipase (41), all of which increase the conductivity of membranes.

EI spectra were modeled using the equivalent circuit model (ECM) shown in the inset in Fig. 5. The stBLM is represented by a constant phase element (CPE_{stBLM}), whose impedance is defined as

$$Z_{\mathrm{CPE}} = 1/(|CPE|(\mathrm{i}\omega)^{\alpha}), \tag{1}$$

where $|CPE|$ and α are the coefficient and the phase of the constant-phase element, i is the imaginary unit, and $\omega = 2\pi f$ is the cyclic frequency. The relevance and significance of this model were discussed earlier (40). Confidence limits of the parameters are quantified by the covariance matrices of the Levenberg-Marquardt algorithm employed in the nonlinear χ^2 minimization. Representative results of the modeling for DOPC-based stBLMs are shown in Table 4. The mean values of $|CPE|$ and α for the as-prepared stBLMs are 0.676 ± 0.015 μFcm^{-2} s$^{\alpha-1}$ and 0.987 ± 0.002, respectively, determined from $n = 29$ independent measurements. The value of α suggests that the stBLMs exhibit nearly ideal capacitive behavior, and therefore, $CPE_{\mathrm{stBLM}} \approx C_{\mathrm{stBLM}}$, the membrane capacitance. A detailed interpretation of these results in connection with structural data obtained from NR experiments enables us then to deduce molecular-scale models for the impact of Aβ-oligomers on membrane properties, as presented in the Discussion section.

It has been reported that amyloids induce conductance pathways through membranes (21,23,24). These defects were interpreted as being similar to those created by ionophores such as gramicidin (38) or ion channels such as αHL (28). In the ECM in Fig. 5, such pathways are represented by another constant-phase element (CPE_{def}) in series with a resistor, R_{def}. As shown earlier, such a model describes well the intrinsic conductance properties of functionally reconstituted αHL ion channels in stBLMs (43). Hence, the conductance,

$$Y_{\mathrm{A}\beta} = R_{\mathrm{def}}^{-1}, \tag{2}$$

may be a reasonable descriptor of changes in the transport properties of the membrane induced by soluble Aβ_{1-42}-oligomers. The conductance, $Y_{\mathrm{A}\beta}$, and membrane capacitance, C_{stBLM}, of stBLMs completed with DOPC are plotted in Fig. 6 as a function of c_p, the peptide concentration in the aqueous bulk reservoir. C_{stBLM} is linear in c_p. Because membrane thinning is negligible in this concentration range (Table 1), any rise in C_{stBLM} derives from an increase of the membrane's dielectric constant, $\varepsilon_{\mathrm{hc}}$, due to insertion of peptide, which has a higher permeability than alkane. This suggests that C_{stBLM} is also linear to c_p^{stBLM}—the peptide concentration within the membrane—and, consequently, $c_p^{\mathrm{stBLM}} \propto c_p$. On the other hand, Fig. 6 shows that $Y_{\mathrm{A}\beta}$ is nonlinear in c_p, and therefore presumably also nonlinear in c_p^{stBLM}. In fact, the isotherm deviates significantly from Langmuir-type behavior, both in stBLMs and free-standing

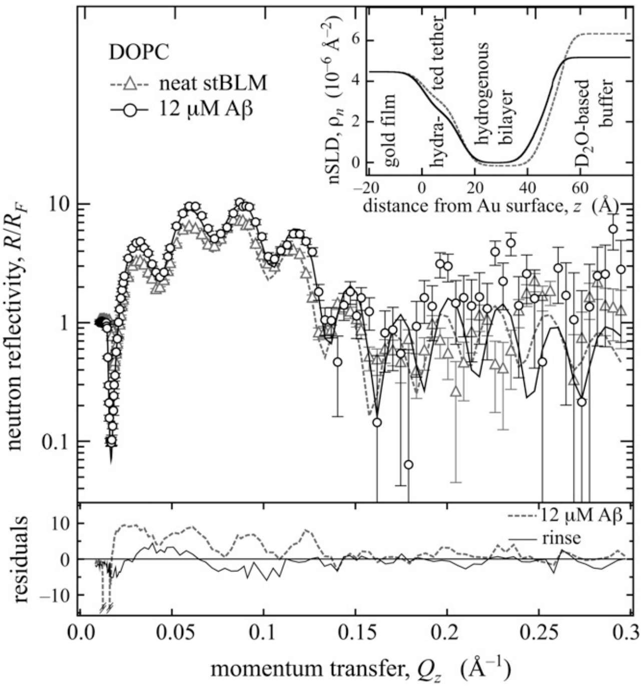

FIGURE 3 Neutron reflection of an stBLM (WC14/βME = 3:7 + DOPC), and changes in bilayer structure introduced by $A\beta_{1-42}$-oligomers. Out of a multitude of NR data sets collected with the same bilayer with various solvent contrasts, two exemplary data sets (as-prepared stBLM and the same stBLM in contact with dissolved Aβ-oligomers, $c_p = 12\ \mu M$ of peptide) are shown in the main panel. Both data sets were measured in D_2O-based buffer. Because peptide in H_2O was added to the buffer, its nSLD is lower than that of the peptide-free buffer (*upper inset*). The resulting difference in scattering power of the solvent leads to a difference in nSLD at the location of the HEO tether, showing that the tether region is hydrated. Other details of the presentation are as described for Fig. 2. A color version of this figure is available in Data S1.

BLMs: $Y_{A\beta}^{-1}$ vs. c_p^{-m} is linear for $m \approx 2$ (instead of $m = 1$, as expected for a Langmuir isotherm), suggesting cooperative effects and/or conformational changes of the $A\beta_{1-42}$-oligomer particles as they transfer from the aqueous to the hydrocarbon environment.

Conductance of free-standing bilayer lipid membranes

Fig. 7 shows Aβ-oligomer-induced current-voltage (I/U) curves through free-standing BLMs as a function of temperature. All curves show the typical exponential shape for activated charge translocation with nearly linear portions near the origin ($|U| \leq 30$ mV (Fig. 7, *inset*)). This inner part of the curves was used to estimate the zero-voltage conductances of the BLMs. Representative data are summarized in Table 5. The increase of the Aβ-induced conductance is superlinear, and a strong temperature dependence—a factor of ~2 per 10°C—indicates a high activation energy of the ion transfer through the membrane.

The ion current induced by Aβ-oligomers across free-standing BLMs was measured as a function of lipid composition. Fig. 8 displays bilayer currents, $I_{A\beta}$, vs. c_p for DOPC, DPhyPC, and their equimolar mixture. Their c_p dependence is nonlinear, with $I_{A\beta}^{-1}$ vs. c_p^{-m} linear for $m \approx 2.3$, which is quantitatively similar to those observed with stBLMs (Fig. 6). Just as the stBLM response is a function of membrane composition seen in NR, the peptide-induced currents show a strong dependence on the phospholipid chain constitution. As the membrane composition is changed from DPhyPC to DOPC, the induced currents increase by a factor of ~20 for a given c_p. Similar effects were observed in the EI spectra of stBLMs, though the differences between saturated and unsaturated chains were smaller, amounting to a factor of only 3–4 (data not shown).

Activation energies of ion transfer across membranes

In view of the remarkable temperature dependence of ion transport through BLMs shown in Fig. 7, EI spectra of stBLMs affected by soluble $A\beta_{1-42}$-oligomers were also determined as a function of T. As with BLMs, a temperature

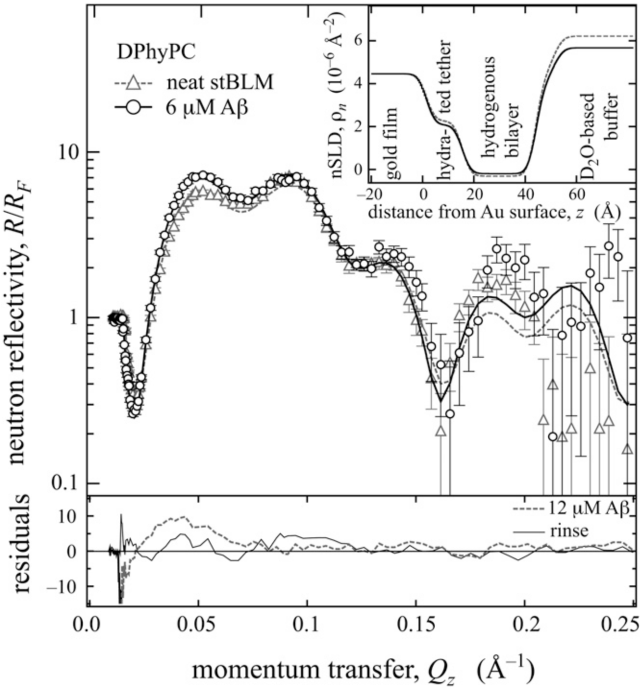

FIGURE 4 Neutron reflection of an stBLM (WC14/βME = 3:7 + DPhyPC), and changes in bilayer structure introduced by $A\beta_{1-42}$-oligomers. Out of a multitude of NR data sets collected with the same bilayer with various solvent contrasts, two exemplary data sets (as-prepared stBLM and the same stBLM in contact with dissolved Aβ-oligomers, $c_p = 6\ \mu M$ of peptide) are shown in the main panel. Both data sets were measured in D_2O-based buffer. Because peptide in H_2O was added to the buffer, its nSLD is lower than that of the peptide-free buffer (*upper inset*). The resulting difference in scattering power of the solvent leads to a difference in nSLD at the location of the HEO tether, showing that the tether region is hydrated. Other details of the presentation are as described for Fig. 2. A color version of this figure is available in Data S1.

TABLE 2 **Model parameters describing changes of an stBLM structure (WC14/βME = 3:7 + DOPC) upon incubation with soluble prefibrillar Aβ_{1-42}-oligomers**

	Neat bilayer	Change from neat bilayer	6 μM Aβ_{1-42}	12 μM Aβ_{1-42}	Rinse
Thickness of tether layer (Å)			11.3 ± 1.0		
Thickness of both bilayer leaflets (Å)	31.0 ± 0.6	Change:	−2.4 ± 0.6	−3.8 ± 0.6	0.0 ± 0.6
Thickness of headgroup layer (Å)			7.0 (fixed)		
Volume fraction of tether in layer			0.59 ± 0.02		
Volume fraction of inner lipid leaflet	1.00 ± 0.02	Change:	−0.01 ± 0.02	0.00 ± 0.03	−0.01 ± 0.02
Volume fraction of outer lipid leaflet	1.00 ± 0.02	Change:	0.00 ± 0.02	0.00 ± 0.03	−0.02 ± 0.02
Volume fraction of outer headgroup	0.66 ± 0.10	Change:	0.05 ± 0.10	+0.05 ± 0.10	−0.02 ± 0.10
nSLD of both lipid leaflets (10^{-6} Å^{-2})	−0.15 ± 0.08	Change:	+0.15 ± 0.06	+0.19 ± 0.06	+0.02 ± 0.06
Bilayer roughness (Å)			6.5 ± 2.2		
χ^2			3.30		

increase leads to pronounced increases of stBLM conductances (Fig. 9). To be specific, both the plateau in the $|Z(f)|$ plot and the phase minimum move toward higher frequencies (data not shown). Modeling of the spectra facilitates a determination of R_{def} and, consequently, an assessment of the temperature-dependence of the conductance changes in the stBLMs.

Temperature effects on stBLM and BLM conductances were determined at $c_{\mathrm{p}} = 1.6$ μM for stBLMs and at $c_{\mathrm{p}} =$ 1 and 2 μM for BLMs. Results are summarized in Fig. 9 and quantified in Table 6. In the figure, Arrhenius plots of stBLM and BLM conductances in the presence of Aβ_{1-42}-oligomers are compared with those for the ion transport in bulk electrolyte and across stBLMs reconstituted with αHL. The slopes of the Arrhenius plots yield activation energies (E_{a}) for ion conductance in the presence of Aβ_{1-42}-oligomers of $E_{\mathrm{a}} \approx$ 37 kJ/mol for a DOPC stBLM; $E_{\mathrm{a}} \approx 46$ kJ/mol at 1 μM peptide and $E_{\mathrm{a}} \approx 33$ kJ/mol at 2 μM peptide for free-standing DOPC BLMs (Table 6). These values are much lower than the activation energies for bare ions to cross neat lipid bilayers, but much larger than those for ion transport in bulk water. In comparison, the activation energy for ion transport through αHL is also significantly lower, $E_{\mathrm{a}} \approx 10$ kJ/mol—closer to the value for ion transport through bulk solvent. E_{a} for the Aβ-induced membrane conductivity itself depends pronouncedly on peptide concentration. In connection with the nonlinear relation, $Y_{\mathrm{A}\beta}(c_{\mathrm{p}})$, shown in Fig. 6, this suggests that the amyloid properties within the membrane change in a concentration-dependent manner.

DISCUSSION

The different model systems investigated in this work, and the measurement techniques employed in their study, are well connected. The combined application of EIS and NR is highly synergetic and provides insight into physical models of the bilayers, and the direct comparison of conductivity measurements and EIS link ion transfer across free-standing bilayers and surface-stabilized membranes. As we show below, there is quantitative agreement between these results. The biophysical effects we report here occur at Aβ concentrations similar to those at which characteristic increases in the membrane conductance of patch-clamped cells were reported in other studies (15,17). Moreover, shifts of the gating properties of voltage-dependent channels (56), as well as cell lysis in tissue culture (57), occur at similar peptide concentrations. We therefore argue that the mechanism by which Aβ-oligomers induce electrical and structural changes in membranes may have significance for the understanding of toxic effects exerted on cellular systems. We first discuss structural implications of the NR results, then, more quantitatively, the electrical effects of Aβ-oligomers on membranes;

TABLE 3 **Model parameters describing changes of an stBLM structure (WC14/βME = 3:7 + DPhyPC) upon incubation with soluble prefibrillar Aβ_{1-42}-oligomers**

	Neat bilayer	Change from neat bilayer	6 μM Aβ_{1-42}	Rinse
Thickness of tether layer (Å)		14.0 ± 1.5		
Thickness of both bilayer leaflets (Å)	28.6 ± 1.4	Change:	+0.2 ± 0.4	−0.4 ± 0.4
Thickness of headgroup layer (Å)		7.0 (fixed)		
Volume fraction of tether in layer		0.66 ± 0.04		
Volume fraction of inner lipid leaflet		1.00 ± 0.04		
Volume fraction of outer lipid leaflet		1.00 ± 0.01		
Volume fraction of outer headgroup		0.42 ± 0.12		
nSLD of both lipid leaflets (10^{-6} Å^{-2})	−0.31 ± 0.09	Change:	+0.12 ± 0.05	−0.02 ± 0.05
Bilayer roughness (Å)		6.4 ± 3.1		
χ^2		3.06		

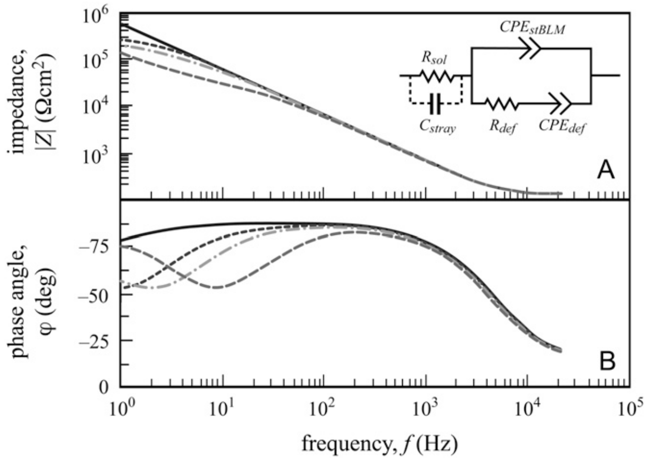

FIGURE 5 Modulus (*A*) and phase angle (*B*) of electrochemical impedance spectra of an stBLM (WC14/βME = 3:7 + DOPC) in phosphate-buffered NaCl (0.1 M), pH 7.4, as a function of peptide concentration for no peptide (*solid line*); 0.48 μM A$\beta_{1\text{–}42}$ (*short-dashed line*); 0.75 μM A$\beta_{1\text{–}42}$ (*dash-dotted line*); 1.61 μM A$\beta_{1\text{–}42}$ (*long-dashed line*). (*Inset*) ECM used to model stBLM data such as those shown in the main panel. *CPE*, constant phase element; subscript ''def'', peptide-induced defect conductance pathways. See text for details.

finally, we comment on implications of these results for our understanding of the mechanism by which Aβ affects membranes, specifically in light of the amyloid channel hypothesis.

Both bilayer leaflets respond similarly to peptide incubation

Fig. 10 shows changes in nSLD (Fig. 10 *A*) and bilayer thickness (Fig. 10 *B*) of deuterated stBLMs due to their exposure to soluble Aβ-oligomers. Because the thickness parameters for the inner and outer leaflets were observed to be highly correlated in the fits, they were constrained to be identical in the model. On the other hand, the nSLDs of the two leaflets, well discriminated due to their distinct isotopic composition, develop differently as a function of c_p. However, this apparent difference vanishes if one compares the scattering-length area density,

$$\rho_n^a = \rho_n \times d, \qquad (3)$$

TABLE 4 EIS model fits for an stBLM (WC14/βME = 3:7 + DOPC) as prepared and after incubation with soluble prefibrillar A$\beta_{1\text{–}42}$-oligomers

	Neat bilayer	1.61 μM A$\beta_{1\text{–}42}$	Rinse
CPE_{stBLM} (μF/cm^{2}s$^{(\alpha-1)}$)	0.676 ± 0.015	0.743 ± 0.018	0.672 ± 0.024
α_{stBLM}	0.987 ± 0.002	0.979 ± 0.002	0.985 ± 0.002
CPE_{def} (μF/cm^{2}s$^{(\alpha-1)}$)	1.01 ± 0.22	2.36 ± 0.46	1.11 ± 0.21
α_{def}	0.52 ± 0.08	0.93 ± 0.04	0.55 ± 0.06
R_{def} (kΩcm^2)	933 ± 110	9.6 ± 2.7	645 ± 124

Model fits are to the ECM shown in Fig. 5; $f = 1$ Hz to 33 kHz. Data are expressed as averages ± standard deviations from multiple measurements ($n > 10$).

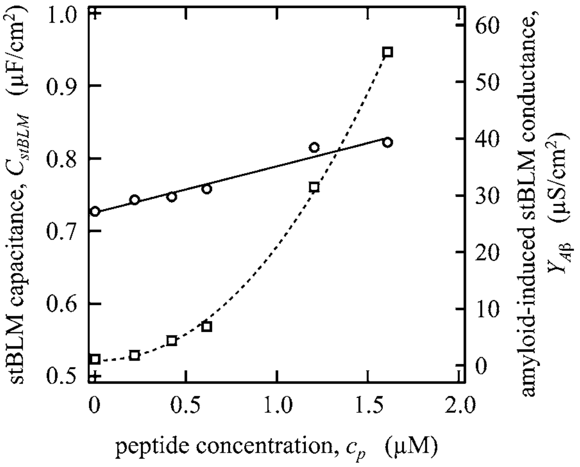

FIGURE 6 Impact of soluble prefibrillar A$\beta_{1\text{–}42}$-oligomers on membrane capacitance and conductance in an stBLM (WC14/βME = 3:7 + DOPC; 0.1 M NaCl, pH 7.5) as a function of peptide concentration, measured on one single bilayer. The impact on stBLM capacitance (*circles/solid line*) and stBLM conductance (*squares/dashed line*) is shown; circles and squares are best-fit parameters from a model (ECM in Fig. 5, *inset*) that describes data sets such as those shown in the main panel of Fig. 5.

which is a measure of inserted material per unit area and is shown in Fig. 10 *C* as a function of c_p. The nearly perfect coincidence of ρ_n^a in both leaflets at any peptide concentration indicates that both monolayers are similarly affected by the peptide.

From these results, the impact of A$\beta_{1\text{–}42}$-oligomers on the DMPC-d$_{54}$ bilayer can be summarized as follows: at $c_p = 2$ μM, no geometrical changes of the membrane are detected. However, the nSLD of both lipid leaflets rises by $0.29 \pm 0.09 \times 10^{-6}$ Å^{-2}. This shows conclusively that there is incorporation of peptide material into the membrane, accompanied by an increase of the lipid packing density. Because

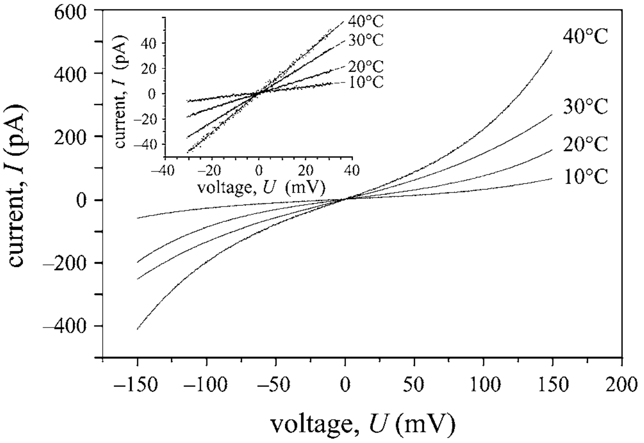

FIGURE 7 Temperature dependence of current-voltage curves recorded on free-standing DOPC BLMs (10 mM KCl, 1 mM HEPES-Tris, pH 7.5) incubated with soluble prefibrillar A$\beta_{1\text{–}42}$-oligomers at a total peptide concentration of 1 μM. Voltage scan rate, 30 mV/s. (*Inset*) Enlarged view of the data in the main panel near zero voltage.

TABLE 5 Zero-voltage conductances of free-standing BLMs as a function of *T*

	Specific conductance, Y (μS cm^{-2})	
Temperature, T (°C)	1 μM A$\beta_{1–42}$	2 μM A$\beta_{1–42}$
10	0.49	3.84
20	1.14	5.73
30	1.68	8.10
40	3.49	15.1

The values are calculated from $U \rightarrow 0$ in the current-voltage curves shown in Fig. 7.

the nSLD of the peptide is substantially lower than that of perdeuterated alkane, a mere replacement of lipid by peptide would be expected to reduce the nSLD of the bilayer core. Fig. 10 *A* shows that the opposite is true. Estimating the peptide nSLD to be $\rho_n = 2.1 \times 10^{-6}$ Å^{-2}, the volume fraction of peptide material within the bilayer is estimated to amount to ~14%. This model assumes that the number of lipids/unit area remains constant. However, a fluid bilayer may respond to peptide-induced changes in lipid conformation—affecting the area/lipid—with lateral flow, depositing excess lipid in reservoirs at defect sites (or retrieving material from such sites). For example, if due to a peptide-induced increase in local-disorder lipid material expanded laterally, the estimate for ρ_n^a is too low. Conversely, the estimate is too high if peptide insertion leads to lipid compaction. Exposure to increasingly larger amyloid concentrations will in that case eventually lead to a situation where membrane compaction can no longer be compensated for by the influx of lipid along the bilayer plane—which might explain the observed membrane thinning at $c_p = 6$ μM and $c_p = 12$ μM.

The nSLD of the outer lipid leaflet increases further by $\Delta\rho_n = 0.49 \pm 0.11 \times 10^{-6}$ Å^{-2} upon raising the peptide concentration in the buffer to 6 μM, and saturates at this level. On the other hand, the nSLD of the inner lipid leaflet decreases gradually from its peak value reached at $c_p = 2$ μM. This difference in behavior between the two membrane leaflets is a consequence of the thinning of the membrane and the distinct starting values of the nSLDs in both leaflets due to different degrees of deuteration. The apparent discrepancy is reconciled if one evaluates the neutron scattering length area densities: ρ_n^a is expected to change equally in both leaflets if they are affected by the same influx or outflux of deuterated lipid (which is the only mobile lipid species). This is in fact what was observed (Fig. 10 *C*). In conclusion, this experiment shows unmistakably that 1), peptide material inserts into the membrane in significant amounts; 2), peptide material affects both bilayer leaflets similarly; and 3), lipid is not simply replaced by the peptide but is, rather, compacted in its local density—at least on average within the plane of the membrane.

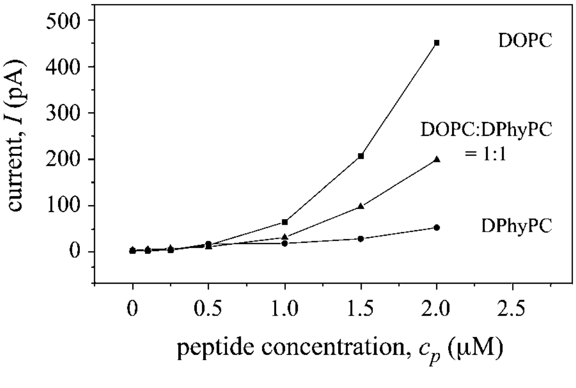

FIGURE 8 Effect of soluble prefibrillar A$\beta_{1–42}$-oligomers on the conductance of free-standing BLMs (10 mM KCl, 1 mM HEPES-Tris, pH 7.5, $T =$ 25°C) as a function of lipid composition. Voltage was +150 mV for all measurements.

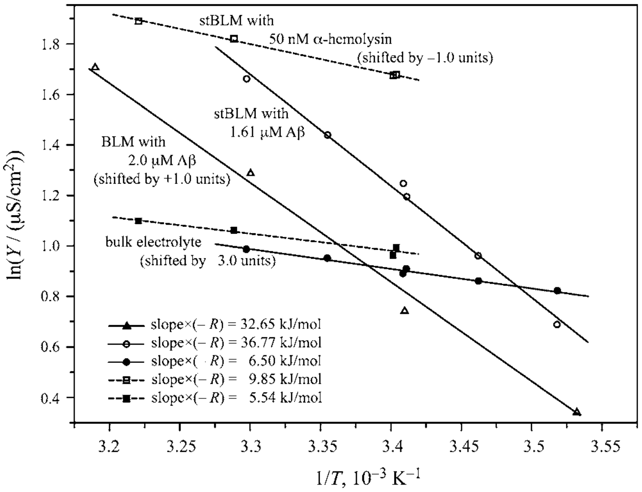

FIGURE 9 Arrhenius plots of ion conductance across bilayers induced by soluble prefibrillar A$\beta_{1–42}$-oligomers or by α-hemolysin, and in the electrolytes bathing these bilayers. In stBLMs, the conductance was derived from modeling EIS data with the ECM (Fig. 5, *inset*). Therefore, bulk electrolyte conductances (*solid squares* and *circles*) and membrane conductances (*open squares* and *circles*) were determined in the same experiment. The stBLM incubated with Aβ (*circles*) was composed of WC14/βME = 3:7 + DOPC; 0.1 M NaCl, pH 7.5. The stBLM reconstituted with αHL (*squares*) was prepared as described (40), and consisted of WC14/βME = 3:7 + DPhyPC. Measurements on free-standing BLMs (*triangles*) were conducted with DOPC membranes in 10 mM KCl, HEPES-Tris, pH 7.4. $R = 8.3145$ J/(mol × K) is the gas constant. Lines are best fits to the data. BLM data for $c_p = 1$ μM are omitted for clarity. BLM and stBLM experiments with A$\beta_{1–42}$-oligomers were conducted on bilayers formed with DOPC, because the response of these bilayers to the peptide is significantly larger than that of membranes formed with DPhyPC (Fig. 8). In contrast, αHL was studied in DPhyPC-based stBLMs, because these were the membranes used for αHL reconstitution in a different investigation (43). From these studies, we concluded that the reconstituted protein forms fully active membrane pores in the stBLMs, which introduce narrow, water-filled channels into bilayers (42). Attempts to reconstitute αHL into DOPC-based stBLMs have so far not been successful in our lab.

NR results for the incubation of fully hydrogenated stBLMs with soluble A$\beta_{1–42}$-oligomers (Figs. 3 and 4) showed small nSLD increases in response to peptide expo-

TABLE 6 Activation energies determined from the Arrhenius plots

System (experimental conditions)	Activation energy, ΔE (kJ/mol)
1.6 μM A$\beta_{1\text{–}42}$-oligomers in stBLMs (EIS, 100 mM NaCl)	36.8
1 μM A$\beta_{1\text{–}42}$-oligomers in BLMs (current, 10 mM NaCl)	46.1
2 μM A$\beta_{1\text{–}42}$-oligomers in BLMs (current, 10 mM NaCl)	32.7
αHL in stBLMs (EIS, 100 mM NaCl)	9.9
100 μM gramicidin D (EIS, 100 mM NaCl)	16.7*
100 mM NaCl solution (EIS)	5.6 . . . 6.5

The Arrhenius plots are shown in Fig. 9. A comparison between Aβ-induced conductances, the conductance induced by the pore-forming α-hemolysin, and the conductance of ions in bulk solution reveals that ion transfer induced by soluble A$\beta_{1\text{–}42}$-oligomers is substantially different from that through αHL.

*See Gervasi and Vallejo (64).

sure (Tables 2 and 3). These changes are consistent with the interpretation, derived from results with deuterated stBLMs, that Aβ-oligomer incorporation into the membrane increases the lipid density. However, such a conclusion cannot be drawn from the DOPC and DPhyPC data alone, because both a peptide-induced lipid compaction and displacement of hydrogenated lipids by peptide without compaction are expected to result in an nSLD increase of a fully hydrogenated lipid bilayer.

Reversibility of A$\beta_{1\text{–}42}$-oligomer effects on membranes upon rinsing

As shown in the residual plots in Figs. 2–4 and Fig. 10, the structural impact of A$\beta_{1\text{–}42}$-oligomers on membranes is almost perfectly reversible upon rinsing. In a similar way, conductivity increases of bilayer induced by the peptide are largely reversed by simply rinsing the membranes with buffer, consistent with earlier reports (17). Moreover, it has been shown that most adverse effects of A$\beta_{1\text{–}42}$-oligomers on membrane and cell models—and even in vivo effects—can be avoided, or even reverted, by exposure to the oligomer-specific antibody, A11, developed in the Glabe lab (14). Although due to the lack of NR experiments with deuterated peptide we do not yet have a detailed molecular-scale picture of the interaction of Aβ-oligomers with the membrane, these findings suggest an intriguing and unusual propensity for adaptation of the peptide aggregates to either the aqueous or the hydrophobic milieus. Clearly, upon transferring from buffer to the membrane interior, Aβ-oligomers must undergo conformation and/or aggregation changes to adapt to the different natures of these molecular environments. The apparent ease of peptide clearance from the membrane, presumably connected with a redispersion into aqueous buffer, then indicates that this interconversion cannot be associated with a large energetic barrier. It is unfortunate that a lack of more detailed structural information prevents us from drawing more rigorous conclusions at this time.

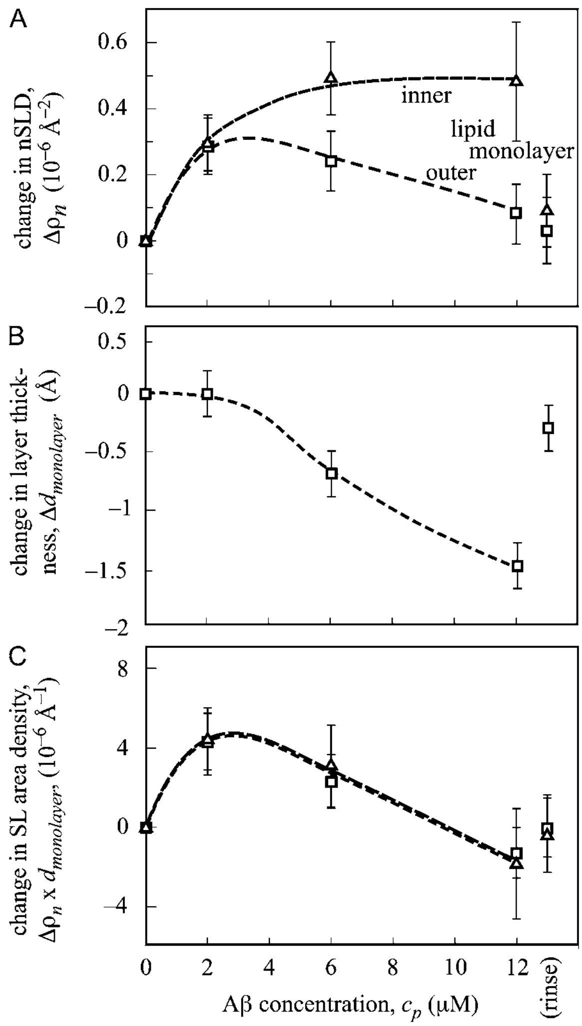

FIGURE 10 Structural changes of an stBLM (WC14/βME = 3:7 + DMPC-d_{54}) incubated with soluble prefibrillar A$\beta_{1\text{–}42}$-oligomers at various concentrations, then rinsed with peptide-free buffer. The plots show the development of model parameters, derived from simultaneous fits to multiple data sets, as a function of c_p. (*A*) Changes in nSLD in apposed bilayer leaflets. The inner and outer bilayer leaflets are represented by triangles and squares, respectively. Note that the baseline nSLD is different in the two leaflets (Fig. 2, *upper inset*). (*B*) Changes in layer thickness, with no distinction between the bilayer leaflets. See Fig. 2 (*upper insets*) for profiles that show the reduction in layer thickness at a peptide concentration c_p = 12 μM. (*C*) Changes in neutron scattering length/unit area, discriminated by apposed leaflets. Triangles and squares are as in *A*. The respective changes for various values of c_p coincide for the two leaflets within confidence limits. Dashed lines are guides for the eye.

Dielectric membrane properties and mechanisms that may compromise barrier function

Earlier results (17), as well as those presented here, suggest that the increased ion conductance of membranes affected by

Aβ-oligomers results from a breakdown of the dielectric barrier that prevents charged species from crossing the lipid bilayer. What is the mechanism of this dielectric breakdown? At least four scenarios are conceivable. 1), Pores or channels may be formed by Aβ-oligomers in the membrane. 2), A mere thinning of the membrane (without the formation of pores), as observed with NR at $c_p > 2\ \mu$M (Fig. 10), could increase ionic permeability. 3), Because proteinaceous material has a larger ε than alkane, incorporation of Aβ-oligomers into the membrane may elevate ε_{hc}, thus reducing the energetic barrier for ion transport. 4), Aβ incorporation into the membrane could also introduce water and increase ε. Even if this did not lead to the formation of contiguous, membrane-spanning water-filled channels, such water-filled pockets might be even more effective than scenario 2 in reducing the energy barrier.

The formation of membrane pores has been a recurring theme in the explanation of the observed increases in bilayer conductivity after incubation with Aβ (21–24,58–60). This possibility has therefore been thoroughly considered in the data interpretation. However, for the membrane model systems and experimental conditions employed here, this scenario is not consistent with the experimental results, even if at first sight circumstantial evidence appeared to point toward channel formation.

For example, our observation of membrane thinning accompanying a conduction increase might be interpreted as a result of amyloid channel formation, since reports in the literature show that pore-forming antimicrobial peptides lead to similar effects (61–63). Nevertheless, the nature of the conductance increase in the systems investigated here is dramatically different from those in other systems interpreted as being due to channel formation (15,17). Moreover, NR does not indicate any increase of water content in the bilayers. Although narrow pores at low concentration in a bilayer may not increase their water content sufficiently to be detected by NR, the activation energy of ion transport across the bilayer (Fig. 9 and Table 6) all but rigorously exclude channel formation in the BLMs and stBLMs we studied. As suggested from its crystal structure (42), and verified in electrophysiology experiments (28), αHL forms well defined water-filled pores in phospholipid bilayers. Ion transport through αHL pores is characterized by about the same activation energy ($E_a \approx 10$ kJ/mol) as ions moving freely in solution bulk ($E_a \approx$ 5 kJ/mol). In distinction, the ion conduction through Aβ-induced pathways has a significantly higher activation energy ($E_a \approx$ 46–33 kJ/mol for stBLMs and BLMs, both composed of DOPC, in the concentration range of 1–2 μM peptide), suggesting a fundamentally different mechanism. As shown in Table 6, the activation energy observed for Aβ_{1-42}-oligomers is not only three times higher than that measured with αHL, but is also significantly higher (more than twofold) than that reported for a different pore, gramicidin D (64), which forms narrower pores (diameter 3–4 Å (65,66)) than αHL (~10 Å). Therefore, we dismiss the formation of pores as the origin of the increase in ion conductivity across the membrane in the model systems studied here under the experimental conditions used.

In a similar way, by virtue of the NR results we can dismiss scenario 4, the possibility that water inclusions contribute significantly to an increase in the dielectric constant of the bilayer. Changes of the water content in the bilayers, if there were any, were <1%, as judged from the models displayed in Tables 1–3. One percent of water in the bilayer would increase the dielectric constant, ε, by <0.8—too little to account for the observed increase in membrane current, as we show below.

Before discussing in detail the most likely amyloid-induced ion transport mechanism(s), we quantify in more detail the dielectric properties of the membrane. Using the membrane thickness derived from NR, we estimate the dielectric constant, ε_{hc}, of the hydrophobic membrane slab as follows. The capacitance of the stBLM is composed of serial contributions from the hydrocarbon (*hc*) slab and the Helmholtz (*H*) capacitance:

$$C_{\mathrm{stBLM}}^{-1} = C_{\mathrm{hc}}^{-1} + C_{\mathrm{H}}^{-1}. \tag{4}$$

On the basis of an approximate value for C_H of 6.25 ± 0.12 μF cm^{-2} with $\alpha = 0.992 \pm 0.001$ ($n = 10$), determined earlier, and the experimental result for C_{stBLM}, we calculate $C_{\mathrm{hc}} \approx 0.76\ \mu$F cm^{-2}. Using Eq. 5,

$$\varepsilon_{\mathrm{hc}} = \frac{C_{\mathrm{hc}} \times d_{\mathrm{hc}}}{\varepsilon_0}, \tag{5}$$

C_{hc} in connection with the experimentally measured thickness, $d_{\mathrm{hc}} = 32.8 \pm 0.5$ Å, yields $\varepsilon_{\mathrm{hc}} \approx 2.8$ for DOPC. An analogous estimate for DPhyPC yields $\varepsilon_{\mathrm{hc}} \approx 2.2$, consistent with the distinct nature of the unsaturated and saturated chains. In what follows, these results for $\varepsilon_{\mathrm{hc}}$ will serve as an experimentally determined basis for the quantification of Aβ-oligomer-induced changes of dielectric membrane properties.

Fig. 6 shows that a pronouncedly nonlinear increase in $Y_{A\beta}$ is accompanied by an increase in C_{stBLM} that is linear in c_p. Because α remains close to unity (Table 4), $CPE_{\mathrm{stBLM}} \approx C_{\mathrm{stBLM}}$ at all c_p. At $c_p = 1.6\ \mu$M, $C_{\mathrm{stBLM}}^{A\beta} = 0.74 \pm 0.02\ \mu$F/cm^2, and with Eq. 4, $C_{\mathrm{hc}}^{A\beta} = 0.84 \pm 0.02\ \mu$F/cm^2 for DOPC membranes affected by Aβ-oligomers, an increase in membrane capacitance of ~11%.

Since we have dismissed the channel scenario, this Aβ-induced conductance increase may be due to either membrane thinning or an increase in $\varepsilon_{\mathrm{hc}}$ or both. Membrane permeability and conductance both scale with the geometric barrier thickness as d_{hc}^{-1} (67,68). In addition, membrane thinning may also affect permeability by lowering the barrier for ion penetration into the hydrophobic core of the bilayer. Image charge effects are the main reason for this reduction but do not change the barrier height significantly in the membrane thickness regime $d_{\mathrm{hc}} \approx 30$ Å (68,69). For example, from the data in Fig. 2 of Neumcke and Läuger (68), we estimate that the hydrophobic barrier is lowered by only 5% as d_{hc} decreases from 60 to 40 Å. In comparison, geometric changes of the bilayer are much smaller here. As seen in Fig. 10, a measurable reduction of d_{hc} is only observed at $c_p > 2$ μM for DMPC. The situation is similar for stBLMs composed of DOPC, where geometrical changes of the membrane were smaller than the confidence limits at $c_p \leq 2$ μM. Consequently, one may with confidence exclude geometric changes of the bilayer thickness as the source of the observed increase in *CPE*. Therefore, we proceed by analyzing quantitatively the possibility of changes of ε_{hc} by peptide insertion as the origin of dielectric breakdown of the membrane barrier.

A uniform increase in membrane dielectric constant is inconsistent with the observed conductivity increase

The dielectric constant, ε_{hc}, has a profound effect on ion permeability across the membrane because of the exponential dependence of the transfer rate on barrier height (70). For monovalent ions, Eq. 6 shows that the ΔG depends on ε_{hc} as

$$\Delta G_{\text{barrier}} = \frac{e^2}{8\pi\varepsilon_0 r_{\text{ion}}}\left(\frac{1}{\varepsilon_{hc}} - \frac{1}{\varepsilon_w}\right) - \frac{e^2}{4\pi\varepsilon_0\varepsilon_{hc}d_{hc}}\ln\left(\frac{2\varepsilon_w}{\varepsilon_w + \varepsilon_{hc}}\right), \tag{6}$$

where ε_w is the dielectric constant of bulk water, e is the elementary charge, and r_{ion} is the ion radius. Equation 6 accounts only for electrostatic contributions to the energy required for transferring an ion into a hydrophobic medium—the Born self-energy—(first term) and a finite-size correction for the hydrocarbon thickness (second term) (68,69). For an order-of-magnitude estimate of Aβ-induced ionic conductance changes, it is sufficient to account only for electrostatic contributions.

From the barrier height, one may further estimate the membrane conductance for monovalent ions:

$$Y = \frac{c_{\text{ion}}F^2}{RT}\frac{\gamma_+ D_+ + \gamma_- D_-}{d_{hc}}, \tag{7}$$

where c_{ion} is the concentration of the electrolyte, R and F are the gas and Faraday constants, respectively, T is temperature, and γ and D are the partition coefficients and diffusion constants of ions in the membrane, respectively. For an ion k, γ is defined as

$$\gamma_k = \exp(-\Delta G_k/RT). \tag{8}$$

As quantified above, $A\beta_{1-42}$-oligomers increase the capacitance of the hydrocarbon membrane core by 11% at $c_p = 1.6$ μM. For the DOPC-based stBLM, Eq. 5 then predicts an increase in ε_{hc} from 2.8 to 3.1. On the other hand, for $\varepsilon_{hc} = 3.1$, Eq. 6 yields an energy barrier, e.g., for chloride anions, ($r_{Cl^-} = 0.181$ nm), $E_a = 107$ kJ/mol, that would leave the membrane practically impermeable. (On the role of Na^+ ions, see the Appendix.) The ionic conductance of such a membrane in 0.1 M NaCl solution would be $Y \ll 1$ μS/cm^2, well below the experimentally observed result. A compelling conclusion from this inconsistency is that Aβ-oligomers cannot affect the membrane dielectric properties uniformly but must exert their impact locally, e.g., by formation of domains where lipids in contact with the peptide may have different properties from lipids far away. It is evident that the increase of ε within Aβ-induced membrane domains is bound to be larger than the expected increase in a hypothetical uniform adsorption model, i.e., $\varepsilon_{hc}^{\text{domain}} \gg 3.1$. The actual value of $\varepsilon_{hc}^{\text{domain}}$ may be estimated by assuming that both Aβ-induced domains and unaffected areas contribute to the membrane capacitance in parallel. If so, then

$$\varepsilon_{hc}^{\text{domain}} = \varepsilon_{hc}^{\text{average}}\frac{(\xi - 1) + \theta}{\theta}x, \tag{9}$$

determines ε within a peptide-induced domain. In Eq. 9 $\varepsilon_{hc}^{\text{average}} = 3.1$ is determined from Eq. 5, θ is the area fraction of membrane domains, $\xi = C_{hc}^{A\beta}/C_{hc}$ is the ratio of specific capacitances of the membrane hydrocarbon slabs within and without peptide, and $x = d_{A\beta}/d_{hc}$ is the corresponding thickness ratio. Vice versa, if $\varepsilon_{hc}^{\text{domain}}$ is known, e.g., from Eq. 6, θ can be determined by inverting Eq. 9.

Implications for membrane physiology

As discussed above, the EIS data yield an estimate of $\xi = 1.11$ at $c_p = 1.6$ μM. Independent NR results show that x in Eq. 9 is ~1 at low c_p for stBLMs of all compositions investigated here. The largest uncertainty concerns the estimate of θ, which cannot be derived with comparable precision from the available data. The most precise NR results—those that involve chain-perdeuterated DMPC—suggest that θ is ~14% of peptide material by volume inside the membrane at $c_p = 2$ μM, if one assumes that the lipid area density in the membrane remains constant; for (hydrogenated) DOPC and DPhyPC, NR results are even less precise. On the other hand, an estimate of θ can be obtained by using the experimentally measured activation energy, $E_a = 36.8$ kJ/mol, as an approximate measure of $\Delta G_{\text{barrier}}$. (On the validity of this approximation, see Appendix) $\varepsilon_{hc}^{\text{domain}} = 8.6$ is determined from Eq. 6. With this value for $\varepsilon_{hc}^{\text{domain}}$, Eq. 9 yields $\theta \approx 0.06$.

A decrease in barrier height from $\Delta G_{\text{barrier}} \gg 100$ kJ/mol for a neat lipid membrane to $\Delta G_{\text{barrier}} \approx 30$–40 kJ/mol will severely compromise the insulation properties of the phospholipid bilayer and result in an increase in membrane conductance. With the results derived in the previous paragraph, we are in a position to estimate membrane conductance from Eq. 7. The finding that a homogeneous membrane model cannot quantitatively account for the observed ion conduction suggests that $A\beta_{1-42}$-oligomers form localized ion conductance pathways within a laterally inhomogeneous membrane. In light of the activation energy results, these pathways cannot, however, be in the form of water-filled membrane-spanning channels. Equation 7 needs to be modified to describe such structural inhomogeneity in a parallel capacitor model. The parameter θ then determines the conductance, $Y = \theta \times Y_{A\beta}$, and yields $Y \approx 180\ \mu S/cm^2$. This value is higher than the experimental data presented in Fig. 6, but is nevertheless a realistic quantitative description of the physical situation, given the substantial uncertainty of some of the input values. A similar analysis for free-standing BLMs in 10 mM electrolyte solution with experimentally determined activation energy $E_a \approx 39.4$ kJ/mol yields a conductance of 6.3 $\mu S/cm^2$—close to the experimental results in Table 5. In BLMs, neither reliable membrane capacitance data nor area fraction estimates exist for the presumed highly conducting membrane domains. In view of the lack of such information, when substituting stBLM results into the estimate for the BLM, we assumed that ε_{hc} increases by 11% in Aβ-affected areas and that the surface fraction of Aβ-induced domains in the membrane is $\theta \approx 0.06$.

Implications for the molecular etiology of Alzheimer's disease

In a recent article, Lashuel and Lansbury reviewed the available evidence for amyloid protofibrils as triggers of age-related neurodegenerative disease by induction of unregulated membrane permeabilization, and they posed the question, Are amyloid diseases caused by aggregates that mimic bacterial pore-forming membranes? (71) In the data presented here, we see significant differences between the molecular mechanisms by which Aβ-oligomers on the one hand and αHL or gramicidin D on the other—prototypical and well-studied membrane pores—affect the membrane ion barrier. There is nevertheless ample evidence, according to the seminal work by Arispe and collaborators (21,72), for amyloid-induced current traces reminiscent of channel-like conductance, as presented in various publications (23,24,73). Complementary morphological studies show AFM images in which donut-shaped peptide aggregates decorate bilayer surfaces (23–25), suggestive of pores perforating the underlying membranes. Further circumstantial evidence from blockage studies with specific metal ions such as Al^{3+}, Zn^{2+}, or Cu^{2+} (72,74,75) lends even more credibility to the amyloid channel hypothesis. One has to keep in mind, however, that studies performed with Aβ until recently were mostly ill defined with respect to the peptide aggregation state, and peptide concentrations used in early work were often extremely high. With the exception of studies on acidic membranes (75), all the ''classical'' studies suggesting pore formation employed peptide concentrations that were at least four times higher (24,25) than those in our experiments—and in many cases substantially higher than that (58,72,73,76). On the other hand, physiological damage to cultured cells has been reported at peptide concentrations comparable to those used in this study (77,78).

The fact that E_a is c_p-dependent and the nearly quadratic dependence of $Y_{A\beta}$ on peptide concentration may hold important clues to the mode of action of the amyloid particles and possible conformational changes they incur in the membrane as a function of c_p. Clearly, we are at best in the very early stages of unraveling the molecular details of how soluble Aβ-oligomers affect membranes, and the c_p dependencies of $Y_{A\beta}$ and E_a in particular require careful investigation.

In addition to the use of well defined Aβ_{1-42}-oligomer preparations at low concentrations, this study also provides a novel approach to investigations on membrane-related issues concerning AD: it encompasses structural and functional characterization of the same physical system, as well as a quantitative comparison of the physical state of membranes before and during incubation with Aβ_{1-42}-oligomers. In contrast, earlier studies often used a variety of more indirect approaches to sample preparation, including the fusion of preformed peptide-lipid assembly products to membranes (72,74), or—as in most AFM studies—premixing of lipid and peptide in dispersions at high peptide/lipid ratios (24,79). Although the impact of these earlier studies on our thinking about amyloid-induced membrane damage cannot be overstated, there has recently been substantial progress in the areas of biochemical synthesis and characterization, and of physical characterization, that make possible a reinvestigation of the underlying mechanisms. Analogous to the realization more than a decade ago that the conspicuous fibrils are not the main pathologically active form of amyloid, another paradigm shift may be just beyond the horizon. One should therefore be open to a reassessment of the arguments about the molecular mechanisms that lead to membrane damage in Alzheimer's disease.

CONCLUSIONS

Arrhenius plots of ion conductance across membranes show that amyloid-induced ion transport is fundamentally different from transport through water-filled αHL pores or gramicidin channels: The activation energies for ion transport through membranes affected by Aβ-oligomers is substantially higher than that found with αHL and gramicidin. In addition, E_a decreases with increasing amyloid concentration, whereas it is approximately constant as a function of αHL concentration. The presence of a large barrier is also inferred from the exponential form of current-voltage curves (Fig. 7), which differ from the near-linear current-voltage characteristics of water-filled, low-barrier αHL pores reconstituted in membranes (80). The combination of precise experimental results for the membrane thickness and specific capacitance is in quantitative accordance with a model in which Aβ_{1-42}-oligomers insert into the bilayer membrane, where they lead to domain formation. Amyloid oligomers may thereby create a mosaic with regions of high local dielectric constant—and consequently low dielectric barrier to ion transfer. Our experiments described here cannot assess the size or distribution of these regions directly, but recent BLM experiments with conductance probes, as well as work on Kv1.3 channels in living cells, suggest that such regions of lower dielectric barrier may alter characteristic properties of a variety of ionophores and physiological ion channels in the membrane. Specifically, Aβ increases the conductance due to nonactin and tetraphenylborate in BLMs and accelerates the gating kinetics of the voltage-gated Kv1.3 channel in rat basophilic leukemia cells (17). Aβ also increases the single-channel conductance of gramicidin channels and increases the efficiency of alamethicin (Y. Sokolov and J. E. Hall, unpublished data). Thus Aβ-oligomers alter the dielectric structure of the lipid bilayer in such a way as to facilitate charge translocation by a variety of conductance mechanisms. We suggest that such effects on the intrinsic membrane conductance and—more likely—on resident voltage-dependent proteins, such as synaptic Ca^{2+} channels (78), may well account for some of the toxic properties of soluble amyloid oligomers in Alzheimer's disease.

APPENDIX

Na^+ ions do not contribute to the ion current across the membrane

Using $r_{Na+} = 0.102$ nm, a membrane thickness, $d_{hc} = 3.28$ nm (Table 2), $T = 293$ K, $c = 10^{-4}$ mol/cm^3, and $\varepsilon_w = 80$, the barrier for Na^+ ions is higher by a factor of ~1.8 than that for Cl^-. Therefore, we assume that Na^+ does not significantly contribute to membrane conductance. We note that this assumption may not be generally valid, because it is not clear whether or not Na^+ dehydrates fully upon partitioning into amyloid-affected membrane domains. In an indirect manner, the absence of reversal potentials (17) indicates that the permeability of Na^+ might be comparable to that of Cl^-. If so, our quantitative estimate for Y may be too low by up to a factor of ~2×.

Relation between activation energy and membrane barrier height

Generally, $E_a \neq \Delta G_{barrier}$. Instead, $E_a \approx \Delta H_{barrier}$, where H is enthalpy. However, because the activation energy is quite significant ($E_a > 10\,RT$), and because Born theory doesn't account for chemical contributions to $\Delta G_{barrier}$, such as the entropy increase associated with ion dehydration upon partitioning into the membrane, we assume that $E_a \approx \Delta G_{barrier}$ is also valid for the purpose of our estimate.

Conductivity of the laterally heterogeneous membrane

Na^+ contributions to the bilayer conductance are neglected (see above). $D = k_BT/(6\pi\eta r_{ion})$ with $r_{Cl^-} = 0.181$ nm yields a diffusion constant for the chloride ion of $D_{Cl^-} = 3.95 \times 10^{-6}$ cm^2/s. With $\Delta G_{barrier} = 36.8$ kJ/mol and a membrane thickness, $d_{hc} = 3.28$ nm, in the presence of Aβ oligomers ($\theta = 0.06$), $Y = 180$ μS/cm^2. The experimental result for the mean conductance of DOPC-based stBLMs obtained with different amyloid oligomer batches was $Y = 104 \pm 22$ μS/cm^2 ($n = 15$) at $c_p = 1.6$ μM. (The data set shown in Fig. 6 was at the low end of those results.) Therefore, the theoretically estimated conductance exceeds this mean value by a factor of 1.8.

SUPPLEMENTARY MATERIAL

To view all of the supplemental files associated with this article, visit www.biophysj.org.

The support of the National Institute of Standards and Technology (U.S. DOC) in providing the neutron research facilities used in this work is gratefully acknowledged. We benefited from helpful discussions with Charlie G. Glabe and valuable advice on Aβ-oligomer preparation from Rakez Kayed and Saskia C. Milton. Paul A. Kienzle provided support for the NR data analysis.

This work was in part funded by the National Science Foundation (CBET-0555201 and 0457148), the National Institutes of Health (1 R01 RR14182), the Lithuanian State Science and Studies Foundation (B38/2008), the American Health Assistance Foundation (A2008-307), and the Alzheimer's Foundation (IIRG-06-26167).

Certain commercial materials, instruments, and equipment are identified in this manuscript to define the experimental procedure as completely as possible. In no case does such identification imply a recommendation or endorsement by the National Institute of Standards and Technology, nor does it imply that the materials, instruments, or equipment identified are necessarily the best available for the purpose.

REFERENCES

1. Cummings, B. J., C. J. Pike, R. Shankle, and C. W. Cotman. 1996. β-amyloid deposition and other measures of neuropathology predict cognitive status in Alzheimer's disease. *Neurobiol. Aging*. 17:921–933.
2. Hardy, J., and D. J. Selkoe. 2002. The amyloid hypothesis of Alzheimer's disease: progress and problems on the road to therapeutics. *Science*. 297:353–356.
3. Lansbury, P. T., and H. A. Lashuel. 2006. A century-old debate on protein aggregation and neurodegeneration enters the clinic. *Nature*. 443:774–779.
4. Hardy, J. A., and G. A. Higgins. 1992. Alzheimers disease: the amyloid cascade hypothesis. *Science*. 256:184–185.
5. Temussi, P. A., L. Masino, and A. Pastore. 2003. From Alzheimer to Huntington: why is a structural understanding so difficult? *EMBO J.* 22:355–361.
6. Lindgren, M., K. Sörgjerd, and P. Hammarström. 2005. Detection and characterization of aggregates, prefibrillar amyloidogenic oligomers, and protofibrils using fluorescence spectroscopy. *Biophys. J.* 88:4200–4212.
7. Lührs, T., C. Ritter, M. Adrian, D. Riek-Loher, B. Bohrmann, H. Döbeli, D. Schubert, and R. Riek. 2005. 3D structure of Alzheimer's amyloid-β(1–42) fibrils. *Proc. Natl. Acad. Sci. USA*. 102:17342–17347.
8. Mastrangelo, I. A., M. Ahmed, T. Sato, W. Liu, C. P. Wang, P. Hough, and S. O. Smith. 2006. High-resolution atomic force microscopy of soluble Aβ42 oligomers. *J. Mol. Biol.* 358:106–119.
9. Chimon, S., M. A. Shaibat, C. R. Jones, D. C. Calero, B. Aizezi, and Y. Ishii. 2007. Evidence of fibril-like β-sheet structures in a neurotoxic amyloid intermediate of Alzheimer's β-amyloid. *Nat. Struct. Mol. Biol.* 14:1157–1164.
10. Kuo, Y. M., M. R. Emmerling, H. C. Lambert, S. R. Hempelman, T. A. Kokjohn, A. S. Woods, R. J. Cotter, and A. E. Roher. 1999. High levels of circulating Aβ42 are sequestered by plasma proteins in Alzheimer's disease. *Biochem. Biophys. Res. Commun.* 257:787–791.
11. Lue, L. F., Y. M. Kuo, A. E. Roher, L. Brachova, Y. Shen, L. Sue, T. Beach, J. H. Kurth, R. E. Rydel, and J. Rogers. 1999. Soluble amyloid β peptide concentration as a predictor of synaptic change in Alzheimer's disease. *Am. J. Pathol.* 155:853–862.
12. McLean, C. A., R. A. Cherny, F. W. Fraser, S. J. Fuller, M. J. Smith, K. Beyreuther, A. I. Bush, and C. L. Masters. 1999. Soluble pool of Aβ

amyloid as a determinant of severity of neurodegradation in Alzheimer's disease. *Ann. Neurol.* 46:860–866.

13. Walsh, D. M., I. Klyubin, J. V. Fadeeva, W. K. Cullen, R. Anwyl, M. S. Wolfe, M. J. Rowan, and D. J. Selkoe. 2002. Naturally secreted oligomers of amyloid β protein potently inhibit hippocampal long-term potentiation in vivo. *Nature.* 416:535–539.
14. Kayed, R., E. Head, J. L. Thompson, T. M. McIntire, S. C. Milton, C. W. Cotman, and C. G. Glabe. 2003. Common structure of soluble amyloid oligomers implies common mechanism of pathogenesis. *Science.* 300:486–489.
15. Kayed, R., Y. Sokolov, B. Edmonds, T. M. McIntire, S. C. Milton, J. E. Hall, and C. G. Glabe. 2004. Permeabilization of lipid bilayers is a common conformation-dependent activity of soluble amyloid oligomers in protein misfolding diseases. *J. Biol. Chem.* 279:46363–46366.
16. Guo, J. P., T. Arai, J. Miklossy, and P. L. McGeer. 2006. Aβ and τ form soluble complexes that may promote self aggregation of both into the insoluble forms observed in Alzheimer's disease. *Proc. Natl. Acad. Sci. USA.* 103:1953–1958.
17. Sokolov, Y., J. A. Kozak, R. Kayed, A. Chanturija, C. Glabe, and J. E. Hall. 2006. Soluble amyloid oligomers increase bilayer conductance by altering dielectric structure. *J. Gen. Physiol.* 128:637–647.
18. Eliezer, D. 2006. Amyloid ion channels: a porous argument or a thin excuse? *J. Gen. Physiol.* 128:631–633.
19. Bucciantini, M., E. Giannoni, F. Chiti, F. Baroni, L. Formigli, J. S. Zurdo, N. Taddei, G. Ramponi, C. M. Dobson, and M. Stefani. 2002. Inherent toxicity of aggregates implies a common mechanism for protein misfolding diseases. *Nature.* 416:507–511.
20. Ambroggio, E. E., D. H. Kim, F. Separovic, C. J. Barrow, K. J. Barnham, L. A. Bagatolli, and G. D. Fidelio. 2005. Surface behavior and lipid interaction of Alzheimer β-amyloid peptide 1–42: a membrane-disrupting peptide. *Biophys. J.* 88:2706–2713.
21. Arispe, N., H. B. Pollard, and E. Rojas. 1993. Giant multilevel cation channels formed by Alzheimer disease amyloid β protein [AβP(1–40)] in bilayer membranes. *Proc. Natl. Acad. Sci. USA.* 90:10573–10577.
22. Kawahara, M., and Y. Kuroda. 2000. Molecular mechanism of neurodegeneration induced by Alzheimer's β-amyloid protein: channel formation and disruption of calcium homeostasis. *Brain Res. Bull.* 53:389–397.
23. Lin, H., R. Bhatia, and R. Lal. 2001. Amyloid β protein forms ion channels: implications for Alzheimer's disease pathophysiology. *FASEB J.* 15:2433–2444.
24. Quist, A., L. Doudevski, H. Lin, R. Azimova, D. Ng, B. Frangione, B. Kagan, J. Ghiso, and R. Lal. 2005. Amyloid ion channels: a common structural link for protein-misfolding disease. *Proc. Natl. Acad. Sci. USA.* 102:10427–10432.
25. Green, J. D., L. Kreplak, C. Goldsbury, X. L. Blatter, M. Stolz, G. S. Cooper, A. Seelig, J. Kistler, and U. Aebi. 2004. Atomic force microscopy reveals defects within mica supported lipid bilayers induced by the amyloidogenic human amylin peptide. *J. Mol. Biol.* 342:877–887.
26. Micelli, S., D. Meleleo, V. Picciarelli, and E. Gallucci. 2004. Effect of sterols on β-amyloid peptide (AβP 1–40) channel formation and their properties in planar lipid membranes. *Biophys. J.* 86:2231–2237.
27. Kawahara, M., Y. Kuroda, N. Arispe, and E. Rojas. 2000. Alzheimer's β-amyloid, human islet amylin, and prion protein fragment evoke intracellular free calcium elevations by a common mechanism in a hypothalamic GnRH neuronal cell line. *J. Biol. Chem.* 275:14077–14083.
28. Bezrukov, S. M., and J. J. Kasianowicz. 1993. Current noise reveals protonation kinetics and number of ionizable sites in an open protein ion channel. *Phys. Rev. Lett.* 70:2352–2355.
29. Terzi, E., G. Hölzemann, and J. Seelig. 1997. Interaction of Alzheimer β-amyloid peptide(1–40) with lipid membranes. *Biochemistry.* 36: 14845–14852.
30. Yip, C. M., and J. McLaurin. 2001. Amyloid-β peptide assembly: a critical step in fibrillogenesis and membrane disruption. *Biophys. J.* 80:1359–1371.
31. Widenbrant, M. J. O., J. Rajadas, C. Sutardja, and G. G. Fuller. 2006. Lipid-induced β-amyloid peptide assemblage fragmentation. *Biophys. J.* 91:4071–4080.
32. Chi, E. Y., C. Ege, A. Winans, J. Majewski, G. Wu, K. Kjaer, and K. Y. C. Lee. 2008. Lipid membrane templates the ordering and induced fibrillogenesis of Alzheimer's disease amyloid-β peptide. *Proteins.* 72:1–24.
33. McIntosh, T. J., and S. A. Simon. 2006. Roles of bilayer material properties in function and distribution of membrane proteins. *Annu. Rev. Biophys. Biomol. Struct.* 35:177–198.
34. Ehehalt, R., P. Keller, C. Haass, C. Thiele, and K. Simons. 2003. Amyloidogenic processing of the Alzheimer β-amyloid precursor protein depends on lipid rafts. *J. Cell Biol.* 160:113–123.
35. Hur, J. Y., H. Welander, H. Behbahani, M. Aoki, J. Frånberg, B. Winblad, S. Frykman, and L. O. Tjernberg. 2008. Active γ-secretase is localized to detergent-resistant membranes in human brain. *FEBS J.* 275:1174–1187.
36. Hattori, C., M. Asai, H. Onishi, N. Sasagawa, Y. Hashimoto, T. C. Saido, K. Maruyama, S. Mizutani, and S. Ishiura. 2006. BACE1 interacts with lipid raft proteins. *J. Neurosci. Res.* 84:912–917.
37. Sackmann, E. 1996. Supported membranes: scientific and practical applications. *Science.* 271:43–48.
38. Cornell, B. A., V. L. B. Braach-Maksvytis, L. B. King, P. D. J. Osman, B. Raguse, L. Wieczorek, and R. J. Pace. 1997. A biosensor that uses ion-channel switches. *Nature.* 387:580–583.
39. Tanaka, M., and E. Sackmann. 2005. Polymer-supported membranes as models of the cell surface. *Nature.* 437:656–663.
40. McGillivray, D. J., G. Valincius, D. J. Vanderah, W. Febo-Ayala, J. T. Woodward, F. Heinrich, J. J. Kasianowicz, and M. Lösche. 2007. Molecular-scale structural and functional characterization of sparsely tethered bilayer lipid membranes. *Biointerphases.* 2:21–33.
41. Valincius, G., D. J. McGillivray, W. Febo-Ayala, D. J. Vanderah, J. J. Kasianowicz, and M. Lösche. 2006. Enzyme activity to augment the characterization of tethered bilayer membranes. *J. Phys. Chem. B.* 110:10213–10216.
42. Song, L., M. R. Hobaugh, C. Shustak, S. Cheley, H. Bayley, and J. E. Gouaux. 1996. Structure of staphylococcal α-hemolysin, a heptameric transmembrane pore. *Science.* 274:1859–1865.
43. McGillivray, D. J., G. Valincius, F. Heinrich, J. W. F. Robertson, D. J. Vanderah, W. Febo-Ayala, I. Ignatjev, M. Lösche, and J. J. Kasianowicz. 2007. Functional reconstitution of *Staphylococcus aureus* α-hemolysin in tethered bilayer lipid membranes. *Biophys. J.* Under revision.
44. Vanderah, D. J., C. W. Meuse, V. Silin, and A. L. Plant. 1998. Synthesis and characterization of self-assembled monolayers of alkylated 1-thiahexa(ethylene oxide) compounds on gold. *Langmuir.* 14:6916–6923.
45. Demuro, A., E. Mina, R. Kayed, S. C. Milton, I. Parker, and C. G. Glabe. 2005. Calcium dysregulation and membrane disruption as a ubiquitous neurotoxic mechanism of soluble amyloid oligomers. *J. Biol. Chem.* 280:17294–17300.
46. Vanderah, D. J., R. S. Gates, V. Silin, D. N. Zeiger, J. T. Woodward, C. W. Meuse, G. Valincius, and B. Nickel. 2003. Isostructural self-assembled monolayers. 1. Octadecyl 1-thiaoligo(ethylene oxides). *Langmuir.* 19:2612–2620.
47. Trassati, S., and O. A. Petrii. 1991. Real surface area measurements in electrochemistry. *Pure Appl. Chem.* 63:711–734.
48. Dura, J. A., D. Pierce, C. F. Majkrzak, N. Maliszewskyj, D. J. McGillivray, M. Lösche, K. V. O'Donovan, M. Mihailescu, U. A. Perez-Salas, D. L. Worcester, and S. H. White. 2006. AND/R: a neutron diffractometer/reflectometer for investigation of thin films and multilayers for the life sciences. *Rev. Sci. Instrum.* 77: 074301.
49. Als-Nielsen, J., and K. Kjaer. 1989. X-ray reflectivity and diffraction studies of liquid surfaces and surfactant monolayers. *In* Phase Transitions in Soft Condensed Matter. T. Riste and D. Sherrington, editors. Plenum Press, New York. 113–138.

50. Kienzle, P. A., M. Doucet, D. J. McGillivray, K. V. O'Donovan, N. F. Berk, and C. F. Majkrzak. 2000–2006. ga_refl, http://www.ncnr.nist.gov/reflpak/garefl.html.

51. Parratt, L. G. 1954. Surface studies of solids by total reflection of x-rays. *Phys. Rev.* 95:359–369.

52. Vaknin, D., K. Kjaer, J. Als-Nielsen, and M. Lösche. 1991. Structural properties of phosphatidylcholine in a monolayer at the air/water interface. Neutron reflection study and reexamination of x-ray reflection experiments. *Biophys. J.* 59:1325–1332.

53. Wiener, M. C., and S. H. White. 1991. Fluid bilayer structure determination by the combined use of x-ray and neutron diffraction. II. ''Composition-space'' refinement method. *Biophys. J.* 59:174–185.

54. Cornell, B. A., G. Krishna, P. D. Osman, R. D. Pace, and L. Wieczorek. 2001. Tethered-bilayer lipid membranes as a support for membrane-active peptides. *Biochem. Soc. Trans.* 29:613–617.

55. Glazier, S. A., D. J. Vanderah, A. L. Plant, H. Bayley, G. Valincius, and J. J. Kasianowicz. 2000. Reconstitution of the pore-forming toxin α-hemolysin in phospholipid/18-octadecyl-1-thiahexa(ethylene oxide) and phospholipid/*n*-octadecanethiol supported bilayer membranes. *Langmuir.* 16:10428–10435.

56. Kozak, J. A., Y. Sokolov, R. Kayed, C. Glabe, and J. E. Hall. 2007. Multiple effects of soluble amyloid peptide oligomers on human potassium channels. *Biophys. J.* Supplement. Abstract 393A.

57. Chong, Y. H., Y. J. Shin, E. O. Lee, R. Kayed, C. G. Glabe, and A. J. Tenner. 2006. ERK1/2 activation mediates Aβ oligomer-induced neurotoxicity via caspase-3 activation and tau cleavage in rat organotypic hippocampal slice cultures. *J. Biol. Chem.* 281:20315–20325.

58. Hirakura, Y., M. C. Lin, and B. L. Kagan. 1999. Alzheimer amyloid Aβ1–42 channels: Effects of solvent, pH, and Congo Red. *J. Neurosci. Res.* 57:458–466.

59. Jang, H., J. Zheng, and R. Nussinov. 2007. Models of β-amyloid ion channels in the membrane suggest that channel formation in the bilayer is a dynamic process. *Biophys. J.* 93:1938–1949.

60. Kagan, B. L., Y. Hirakura, R. Azimov, R. Azimova, and M. C. Lin. 2002. The channel hypothesis of Alzheimer's disease: current status. *Peptides.* 23:1311–1315.

61. Heller, W. T., A. J. Waring, R. I. Lehrer, T. A. Harroun, T. M. Weiss, L. Yang, and H. W. Huang. 2000. Membrane thinning effect of the β-sheet antimicrobial protegrin. *Biochemistry.* 39:139–145.

62. Ludtke, S., K. He, and H. Huang. 1995. Membrane thinning caused by magainin 2. *Biochemistry.* 34:16764–16769.

63. Chen, F. Y., M. T. Lee, and H. W. Huang. 2003. Evidence for membrane thinning effect as the mechanism for peptide-induced pore formation. *Biophys. J.* 84:3751–3758.

64. Gervasi, C. A., and A. E. Vallejo. 2002. Sodium ion transport through gramicidin-doped bilayers. Influences of temperature and ionic concentration. *Electrochim. Acta.* 47:2259–2264.

65. Smart, O. S., J. M. Goodfellow, and B. A. Wallace. 1993. The pore dimensions of gramicidin A. *Biophys. J.* 65:2455–2460.

66. Wallace, B. A. 2000. Common structural features in gramicidin and other ion channels. *Bioessays.* 22:227–234.

67. Walz, D., E. Bamberg, and P. Läuger. 1969. Nonlinear electrical effects in lipid bilayer membranes. 1. Ion injection. *Biophys. J.* 9:1150–1159.

68. Neumcke, B., and P. Läuger. 1969. Nonlinear electrical effects in lipid bilayer membranes. 2. Integration of generalized Nernst-Planck equations. *Biophys. J.* 9:1160–1170.

69. Parsegian, V. A. 1969. Energy of an ion crossing a low dielectric membrane: solutions to four relevant electrostatic problems. *Nature.* 221:844–846.

70. Dilger, J. P., S. G. A. McLaughlin, T. J. McIntosh, and S. A. Simon. 1979. Dielectric constant of phospholipid bilayers and the permeability of membranes to ions. *Science.* 206:1196–1198.

71. Lashuel, H. A., and P. T. Lansbury. 2006. Are amyloid diseases caused by protein aggregates that mimic bacterial pore-forming toxins? *Q. Rev. Biophys.* 39:167–201.

72. Arispe, N., E. Rojas, and H. B. Pollard. 1993. Alzheimer disease amyloid β protein forms calcium channels in bilayer membranes: blockade by tromethamine and aluminum. *Proc. Natl. Acad. Sci. USA.* 90:567–571.

73. Kawahara, M., N. Arispe, Y. Kuroda, and E. Rojas. 1997. Alzheimer's disease amyloid β protein forms Zn^{2+}-sensitive, cation-selective channels across excised membrane patches from hypothalamic neurons. *Biophys. J.* 73:67–75.

74. Arispe, N., H. B. Pollard, and E. Rojas. 1996. Zn^{2+} interaction with Alzheimer amyloid β protein calcium channels. *Proc. Natl. Acad. Sci. USA.* 93:1710–1715.

75. Bahadi, R., P. V. Farrelly, B. L. Kenna, C. C. Curtain, C. L. Masters, R. Cappai, K. J. Barnham, and J. I. Kourie. 2003. Cu^{2+}-induced modification of the kinetics of Aβ(1–42) channels. *Am. J. Physiol. Cell Physiol.* 285:C873–C880.

76. Singer, S. J., and N. N. Dewji. 2006. Evidence that Perutz's double-β-stranded subunit structure for β-amyloids also applies to their channel-forming structures in membranes. *Proc. Natl. Acad. Sci. USA.* 103:1546–1550.

77. Bhatia, R., H. Lin, and R. Lal. 2000. Fresh and globular amyloid β protein (1–42) induces rapid cellular degeneration: evidence for AβP channel-mediated cellular toxicity. *FASEB J.* 14:1233–1243.

78. MacManus, A., M. Ramsden, M. Murray, Z. Henderson, H. A. Pearson, and V. A. Campbell. 2000. Enhancement of $^{45}Ca^{2+}$ influx and voltage-dependent Ca^{2+} channel activity by β-amyloid-(1–40) in rat cortical synaptosomes and cultured cortical neurons. Modulation by the proinflammatory cytokine interleukin-1β. *J. Biol. Chem.* 275:4713–4718.

79. Lin, B., T. L. Morkved, M. Meron, Z. Q. Huang, P. J. Viccaro, H. M. Jaeger, S. M. Williams, and M. L. Schlossman. 1999. X-ray studies of polymer/gold nonocomposites. *J. Appl. Phys.* 85:3180–3184.

80. Misakian, M., J. J. Kasianowicz, B. Robertson, and O. Petersons. 2001. Frequency response of alternating currents through the *Staphylococcus aureus* α-hemolysin ion channel. *Bioelectromagnetics.* 22:487–493.